EFFECT OF ETHANOL ON THE OXIDATIVE REACTIVITY OF GASOLINE DIRECT INJECTION PARTICULATE

A Thesis

by

COLTON TYLER BARNES

Submitted to the Office of Graduate and Professional Studies of
Texas A&M University
in partial fulfillment of the requirements for the degree of

MASTER OF SCIENCE

Chair of Committee,	Andrea Strzelec
Committee Members,	Karl Hartwig
	Bryan Rasmussen
Head of Department,	Andreas A. Polycarpou

August 2017

Major Subject: Mechanical Engineering

ABSTRACT

Exhaust from vehicles is one of the leading contributors of particulate matter (PM) in the atmosphere. PM has been shown to be carcinogenic and to pose a significant risk to human health. Therefore, continuously stricter legislation is being implemented for particulate emissions. Diesel engines are the highest emitters of PM in the exhaust. Due to this, diesel particulate matter has been studied since the 1980's and diesel particulate filters (DPFs) have been in use to reduce diesel PM since 2003. Gasoline Direct Injection (GDI) engines have penetrated the automotive market due to their increased fuel efficiency and high power output. However, due to incomplete fuel volatilization and partially fuel-rich zones, GDI engines tend to produce more particulate matter as compared to conventional spark ignition engines. To aid in reducing PM, GDI engines could benefit from a particulate filter system like diesels have. However, adding a filter in the exhaust system is known to increase backpressure in the exhaust, which is especially problematic for GDI operation and can lead to a fuel penalty.

To minimize the fuel penalty associated with these particulate filters, there is ongoing research to improve both the filter media and the regeneration strategy; the second is the focus of this work. To efficiently regenerate a Gasoline Particulate Filter (GPF), the reactivity of GDI particulate matter must be understood. Previous work has shown that diesel particulate matter formation, nanostructure and reactivity is a function of fuel type. With ethanol being the leading and currently deployed biofuel for gasoline engines, there is interest in studying the effect it has on GDI PM reactivity.

This study investigated the reaction kinetics through Temperature Programmed Oxidation (TPO) and Desorption (TPD) experiments, which yield bulk reactivity characterizations and quantified the volatile organic fraction, respectively. Isothermal Pulsed Oxidation (IPO) experiments determined the activation energies to be 171.7 kJ/mol for GDI E0 PM and 227.4 kJ/mol and for GDI E30 PM. For heterogeneous reactions, such as our solid-gas reactions, surface area is a surrogate measurement for the concentration of the solid phase. BET total surface area measurements determined the specific surface area to be 81.5 m^2/g and 102.25 m^2/g for GDI E0 and E30 PM, respectively.

CONTRIBUTORS AND FUNDING SOURCES

Contributors

This work was supported by a thesis committee consisting of Professors Dr. Andrea Strzelec and Dr. Bryan Rasmussen of the Department of Mechanical Engineering and Professor Dr. Karl Hartwig of the Department of Material Science.

The particulate samples analyzed in this work were provided by Melanie Debusk at Oak Ridge National Lab. Further support was provided by John Storey and Josh Pihl from Oak Ridge

All other work conducted for the thesis was completed by the student independently.

Funding Sources

The research for this project was supported by a grant from NSF and a fellowship from the Texas A&M Mechanical Engineering Department.

TABLE OF CONTENTS

Page

LIST OF FIGURES

Page

LIST OF TABLES

Page

CHAPTER I

INTRODUCTION AND LITERATURE REVIEW

Hydrocarbons are used globally as the main source of fuel in transportation sources. [18] One of the major uses of hydrocarbon fuel in is automotive internal combustion engines (ICEs). An unwanted side effect of hydrocarbon use in ICEs is the emission of particulate matter (PM) into the atmosphere. This complex mixture, of both solid carbonaceous particles and nanoscale droplets, can contain a wide variety of, organic species, metals, and solid particles varying in size from less than 0.1 to approximately 10 μm in diameter. [19] Increased exposure to PM has been linked to numerous adverse health effects, such as cardiovascular disease, chronic obstructive pulmonary disease, asthma, cerebrovascular disease, diabetes mellitus, neurological damage, and preterm birth. [1-4] Specifically, PM is one of the leading causes for infant mortality, and in 2012, was responsible for approximately 3 million premature deaths. [20]

Since exhaust from automobiles is one of the leading contributors of PM in the atmosphere, stricter emission standards are continuously being introduced [21]. In 2015, the US Environmental Protection Agency (EPA) put into effect Tier 3 emissions standards, and the California Air Resources Board (CARB) enacted their LEV III standards[22]. These standards were preceded by the 2014 implementation of the Euro 6 emissions standards in the European Union.

Figure 1 shows a comparison between previous and current emissions standards from the US and Europe. [23]

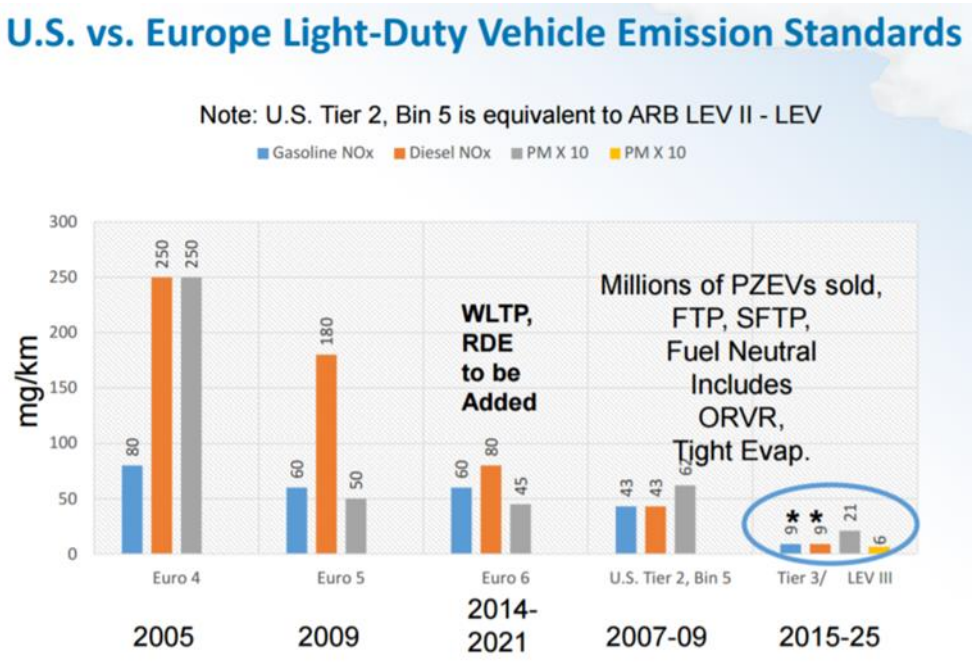

Figure 1: US and Europe Emission Standards [23]

The figure above shows that over time, allowed standards have consistently decreased and that the Tier 3 standards for gasoline and diesel NOx, along with PM, are the most stringent requirements released globally thus far. Additionally, the Tier 3 and LEV III phase-in has called for the constant reduction of exhaust particle number (PN) in Gasoline Direct Injection (GDI) vehicles through year 2025, with Euro 6c, China, and India following, seen below in Figure 2.

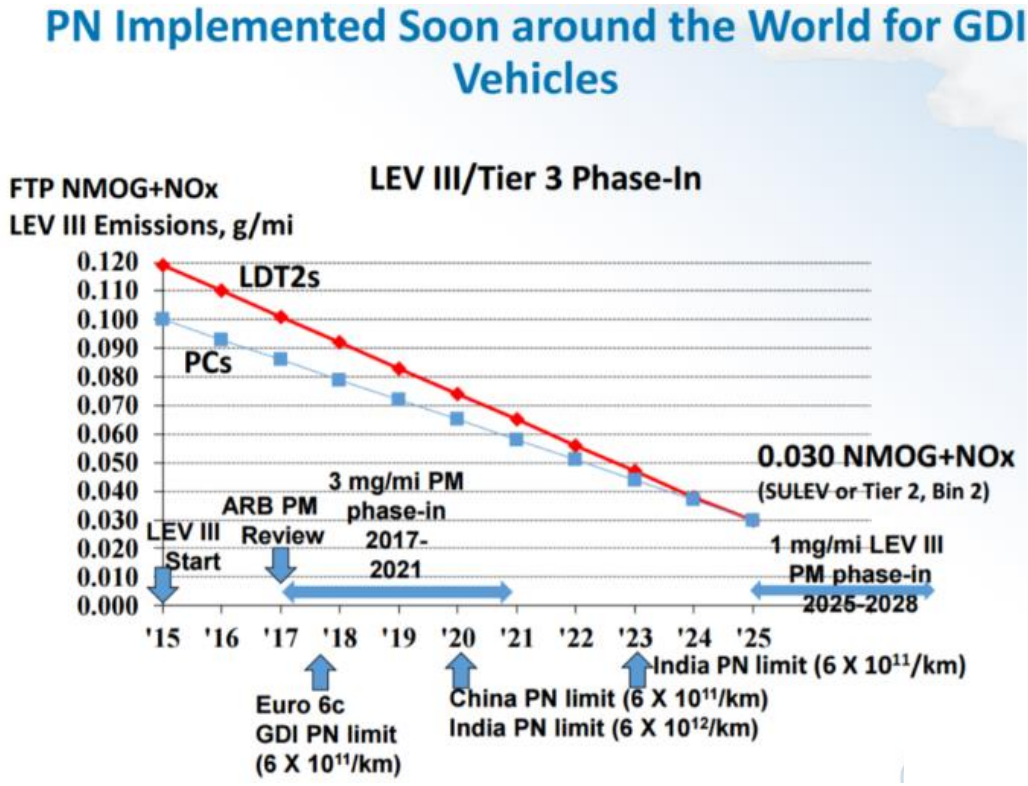

Figure 2: LEV III/Tier 3 PN Limit Phase-In [23]

In addition, Corporate Average Fuel Economy (CAFE) standards in the US warrant improved fuel economy continuously through 2025 for all light duty vehicles. [24] The CAFÉ target curve shows an annual increase in fuel efficiency across all sizes (footprints) of passenger vehicles, supporting the need for the deployment of high efficiency advanced combustion strategies. Improving fuel economy while simultaneously decreasing exhaust emissions presents a crucial challenge for automotive manufacturers around the world. [14]

A large majority of the US passenger fleet are gasoline-powered vehicles, a trend expected to continue in the foreseeable future. In the past few years, Gasoline Direct

Injection (GDI) engines have become increasingly popular in the automotive industry with production of vehicles with GDI engines rising to 45% in 2015. [25] GDI engines utilize an injector inside of the cylinder chamber, which sprays fuel directly into the cylinder, instead of premixing with air in the intake manifold, which happens in traditional Port Fuel Injection (PFI). **Figure 3** shows the varying injection mode types of internal combustion engines and how GDI engines employ benefits from both diesel and traditional gasoline engines. [26] GDI engines have more precise control of injection timing and air-fuel ratio, giving the benefits of increased fuel efficiency, higher power output, and better control over CO_2 emissions. [27, 28]

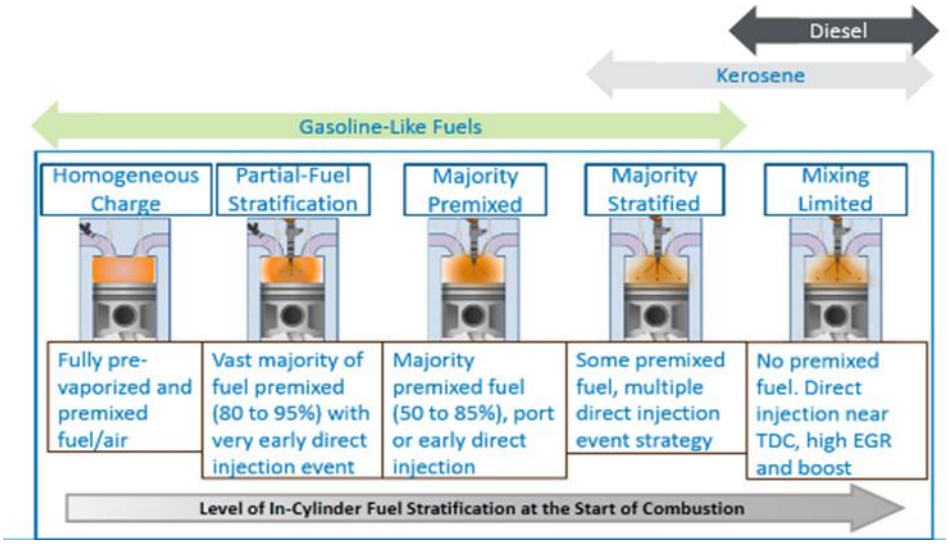

Figure 3: Engine Injection Technology [26]

However, due to the difference in mode of injection, GDI engines produce more particulate matter compared to conventional, homogeneous charge, spark ignition engines. [8-11, 29] One main cause for increased particulate emissions is from fuel impingement on the cylinder, also known as fuel wall wetting. [30] In traditional PFI engines, the air

and fuel are mixed in the intake port, where temperatures are high, allowing the majority of the fuel to vaporize before reaching the cylinder chamber. However, in GDI engines, liquid fuel is sprayed directly in cylinder, where it must vaporize. This causes some fuel to remain liquid and deposit a thin film on the piston top and cylinder wall. This leads to diffusion-controlled burning of the liquid fuel, known as pool fires. [31, 32] Some of this fuel evaporates later during the cycle when temperatures are lower, causing the fuel to not fully oxidize, which leads to increased hydrocarbon emissions. [33] Additionally, since the air and fuel are mixed in cylinder in GDI engines, there is less time for a homogeneous mixture to occur. This creates fuel-rich pockets, which burn disproportionately and form elemental carbon and volatile organic fractions, which increases PM. [32, 34]

Due to the significantly higher concentrations in the exhaust, diesel particulate matter has been studied since the 1980's and technologies have been in use to reduce diesel PM since 2003. [7, 35, 36] Studies have shown that the implementation of a diesel particulate filter (DPF) effectively reduces both PM and particle number (PN) emissions in diesel engines. [37] GDI engines have shown to produce more PM and PN than PFI engines, and significantly more than diesel engines with a DPF, particularly during start up and acceleration. [6, 38] As of now, particulates from GDI engines are unregulated, but as seen in **Figure 4**, they are the next logical targets in particulate reduction. [5]

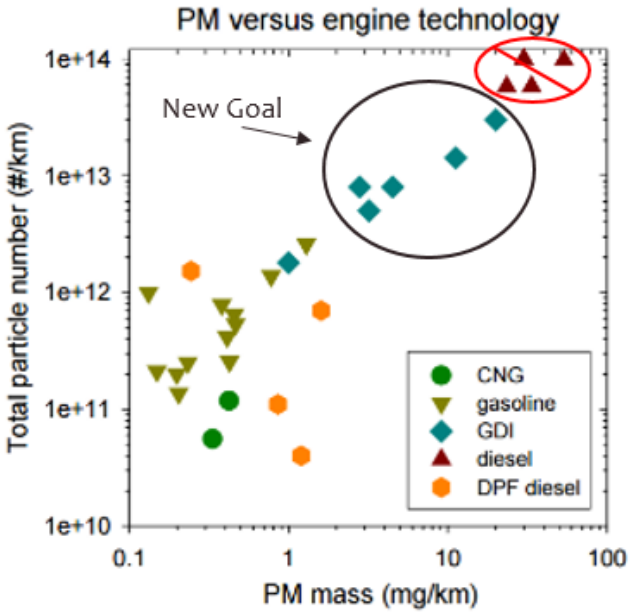

Figure 4: PM Produced vs. Engine Technology [5]

To aid in reducing PM, GDI engines could benefit from a particulate filter system, similar to diesels. [12-14] However, exhaust temperatures and flowrate are higher in GDI engines and adding a filter in the exhaust system will increase backpressure to a higher extent in the exhaust. [12] Since GDI engines are more sensitive to backpressure, this can lead to a penalty in fuel economy, performance, and increased CO_2 emissions. [15] Therefore, performance of a Gasoline Particulate Filter (GPF) will differ from that of a DPF. In order for a GPF to function efficiently, proper management of filtration and regeneration are crucial. Effective regeneration of a GPF requires the understanding of the oxidative reactivity of GDI particulate matter. [13] In order to understand the mechanisms of PM reactivity, the kinetics of the particulate matter must be characterized. Therefore,

gaining better understanding of the oxidation kinetics of GDI PM will lead to further gains in fuel economy and reducing tailpipe emissions.

The passage of the Energy Independence and Security Act (EISA 2007) calls for 36 billion gallons of renewable fuel to be used by 2022, with the majority of this attained from ethanol. [39] The annual increase in biofuels through the year 2022 can be seen in **Figure** 5.

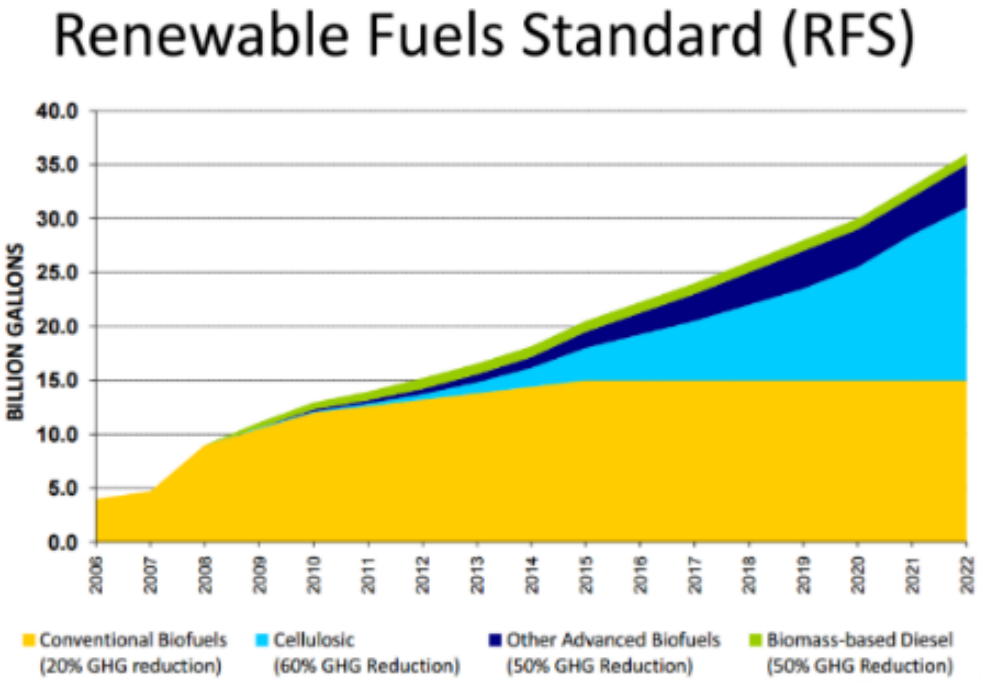

Figure 5: Renewable Fuel Standards through 2022 [40]

The figure shows that the majority of renewable fuel must come from conventional and cellulosic biofuels, namely, ethanol. Ethanol is the leading biofuel of interest for gasoline applications. Additionally, studies have shown that adjusting engine parameters for the inclusion of ethanol in the fuel can increase engine performance, and improved fuel economy. [41] It has been shown for diesels, that particulate matter formation,

nanostructure and reactivity is a function of fuel type. [16, 17] Therefore, there is interest in studying the effect of ethanol on the reactivity of GDI particulate.

In this study, particulate matter generated on a 1.4L GDI engine, from two fuel sources were supplied by Oak Ridge National Laboratory (ORNL), one from pure gasoline (E0) and one from a 30% volumetric blend of ethanol in gasoline (E30). The reaction kinetics for oxidation of GDI particulate matter and the effect of ethanol blending on GDI PM reactivity and structure are examined here.

CHAPTER II

EXPERIMENTAL METHODS

2.1 Experimental Setup

All experiments were performed in a flow-through microreactor, designed and built in the Combustion and Reaction Characterization Laboratory (CRCL) at Texas A&M University (TAMU). The system was constructed in order to combine different types of heterogeneous reaction experimental equipment into one experimental apparatus. The reactor is capable of a variety of experiments including Temperature Programmed Reactions (TPX), BET total surface area measurements, Isothermal Pulsed Oxidation (IPO), and chemisorption.

The reactor consists of two quartz u-tube reactor cells, with thermocouples in each tube to measure the sample bed temperature. A cylindrical, radiant furnace is used to heat each reactor cell and there is a thermocouple wrapped around the u-tube for feedback, in order to regulate the furnace. Reactors 1 and 2 hold the sample in question and an oxidation catalyst, respectively. The oxidation catalyst is a Pt/Al_2O_3 catalyst used to completely convert the products of combustion from the reactor 1 effluent hydrocarbons and CO to CO_2 and H_2O. The exhaust CO_2 content is then measured with a Hiden QGA quadrupole Mass Spectrometer. MKS mass flow controllers regulate the flow of compressed, bottled gases introduced via two manifolds. A fast switching valve directs which manifold flows the gasses. The system is calibrated regularly with 1.5%, 1.0%, 0.75%, 0.5%, 0.25%, 0.125%, and 0.1% CO_2. A Solidworks model of the CRCL Microreactor can be seen in Figure 6.

Figure 6: A Solidworks Model of the CRCL Microreactor [42]

2.2 Experimental Methods

2.2.1 CO_2 Calibration

The partial pressure of CO_2 in the exhaust gas is sampled and analyzed using a Hiden Analytical Quantitative Gas Analysis (QGA) Mass Spectrometer. CO_2 calibrations were conducted bi-monthly to maintain accuracy of experimental results. For the calibration, with Argon as the carrier gas, varying CO_2 concentrations were used in a step-wise manner. The first step of 1.5vol% of CO_2 is held until a flat baseline is stabilized. The vol% is then decreased by 0.5 for the next step and then by 0.25 for the subsequent steps until the concentration is 0.1vol%. Previous calibrations were performed with a higher gas bottle concentration of CO_2 (5.0vol%); however, it was decided lowering the bottle concentration to 1.9vol% would be beneficial. Doing this allows for the final step percentage to be lower (0.1vol%). This low of a concentration equates to 1000ppm of CO_2,

which falls within the range of the TPX experimental results and allows for a more accurate calibration. An example CO_2 calibration can be seen in Appendix A.

2.2.2 Sample Packing

Samples are packed plug-style in the quartz reactor cells. Quartz wool is used to create a bed at the bottom of the tube to keep the sample in the tube. To ensure proper thermal stability, the sample is combined with 1mm diameter Y-ZrO_2 milling beads. Samples masses are typically approximately 10 mg. Quartz wool is then placed over the sample bed to prevent sample loss in case of backflow.

2.2.3 Temperature Programmed Reactions

Three different Temperature Programmed experiments, Oxidation, Desorption, and Oxidation on a previously devolatilized sample (collectively referred to as TPX experiments), were performed to study the bulk reactivity characteristics of the particulate matter samples. These experiments are used to determine the oxidation behavior, volatile organic fraction, and the fixed carbon ratio, respectively.

2.2.3.1 Temperature Programmed Oxidation

Temperature programmed oxidation (TPO) is used to analyze the bulk oxidation behavior of a combustible sample. TPO flows 10% Oxygen in Argon over the sample in reactor 1. The temperature is held for 5 min at 50^{O}C, ramped at 5^{O} per minute to 710^{O}C and held for 15 minutes. The combustion occurs in reactor 1 where the carbon content is burned off and sent to reactor 2 where the oxidation catalyst is held, which converts any CO to CO_2. The amount of CO_2 measured by the Hiden Analytical QGA Mass

Spectrometer quantifies the total carbon content. Figure 7 shows the gas flow path for a TPO experiment.

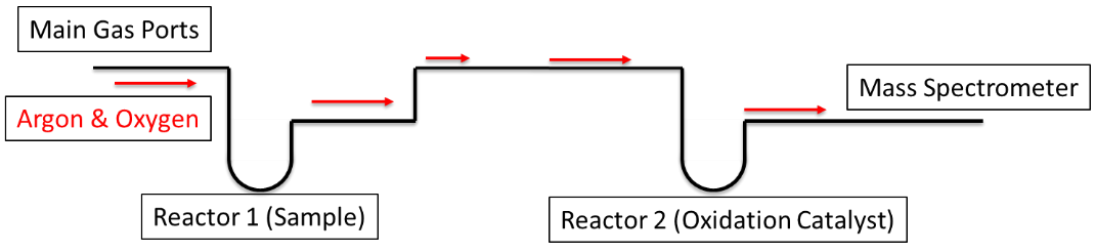

Figure 7: TPO Flow Diagram [42]

2.2.3.2 Temperature Programmed Desorption

Temperature Programmed Desorption (TPD) quantifies the mobile carbon, or volatile organic fraction (VOF) of the particulate matter. This is achieved by only flowing inert Argon over the particulate matter sample while the temperature follows the same ramp as described earlier, allowing the mobile, or volatile carbon to devolatilize over the course of the temperature ramp. [16] In order to quantify the mobile carbon, O_2 is added into the flow after the sample, but before the oxidation catalyst in reactor 2. This allows the volatile hydrocarbon species to combust and allows for the mass spectrometer to measure CO_2. **Figure 8.**

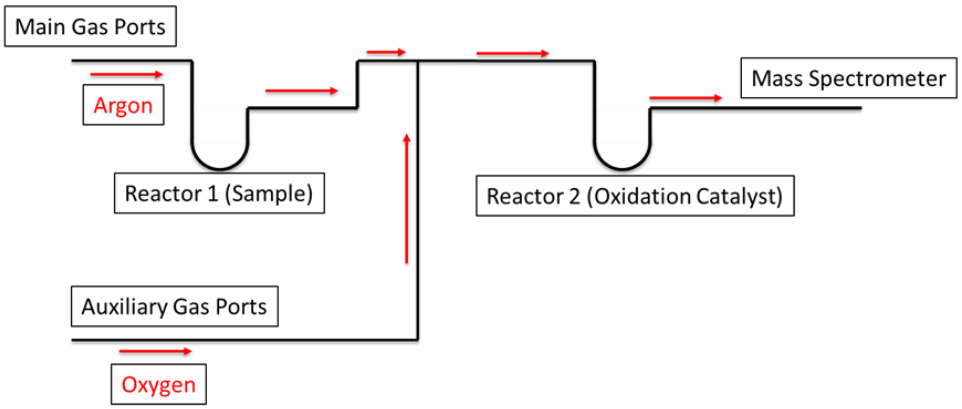

Figure 8: TPD Flow Diagram [42]

2.2.3.3 Temperature Programmed Oxidation on a Devolatilized Sample

This is a TPO performed on a particulate matter sample that has previously undergone a TPD. Due to the mobile carbon content having already been removed by devolatilization (due to the TPD), only the fixed carbon is remaining in the sample held in reactor 1. Performing a TPO on the devolatilized sample allows us to quantify the amount and reactivity of the fixed carbon content. The experiment follows the same process as a TPO, described previously. The gas flow path for this experiment is seen in **Figure 9**

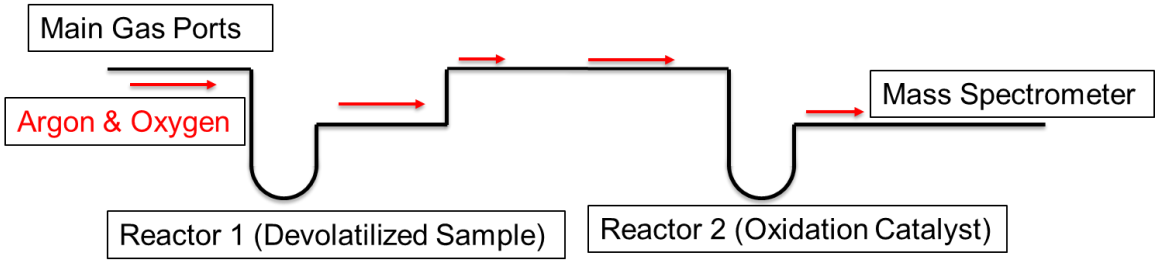

Figure 9: TPO on a Devolatilized Sample Flow Diagram [42]

2.2.4 BET Surface Area Measurements

When performing characterization experiments on a sample undergoing a heterogeneous reaction, a key property to determine is the specific surface area, which is the portion of the solid sample that is available for gas contact, and therefore, reaction. The specific surface area can be described as the quotient of total surface area per unit mass. [43] One way to derive this property experimentally is by adsorption using the Brunauer-Emmett-Teller (BET) theory. [44] The BET theory characterizes porous material by the physical adsorption of an inert gas on a solid surface. This allows for better understanding of the structure and texture of particles.

In these experiments, a particulate sample was prepared as previously described and then placed in reactor 1 with a flowrate of 125 ml/min of Helium. An Argon concentration of 8.5% was introduced into the gas stream, and a baseline was achieved. A vacuum flask of liquid nitrogen is used to decrease the temperature of the flowing Argon, causing it to physisorb (or condense) onto the particulate sample. After 5 minutes, the sample was removed from the liquid nitrogen, allowing the temperature of the Argon to increase and desorb off of the sample. This process is repeated seven more times decreasing the concentration of Argon, by 1% each time, to a final experimental concentration of 1.5%. Compiling the eight data points into a plot and using the measured pressures, allows for the calculation of the specific surface area by the BET method [43].

2.2.5 Isothermal Kinetic Determination of Parameters

In order to determine the activation energy of a sample, experiments evaluating the rate of reaction of sample consumption at a variety of temperatures are essential. Limiting experiments to isothermal, differential measurements lessens the difficulty of calculating kinetic parameters by dissociating the effects of gas parameters. [45, 46]

Isothermal KPD experiments grant the sole focus on the determination of the kinetics of particulate samples. In calculating reaction kinetics, the reaction rate law must be observed to determine the order of the reaction. For a zero-order reaction, the rate is independent of the reaction concentration and remains constant with changing reactant concentrations. Zero-order reactions usually occur for heterogeneous catalysis reactions when the surface is saturated with reactants. The rate law for zero-order reactions is given by

$$r = -\frac{d[C]}{dt} = k[C]^0 = k = constant$$

with *k* being the effective rate constant, which can be determined by plotting concentration vs. time.

A first-order reaction is dependent on only one concentration of a reactant and varies linearly with time. The rate law for first-order reactions is given by

$$r = \frac{d[C]}{dt} = k[C]$$

Integrating this expression yields

$$\ln\left[\frac{C}{C_o}\right] = -kt$$

where the initial concentration is [C_o]. Plotting ln[C] vs. time gives a linear plot with a slope of -k.

If the reaction is dependent on the concentration of a reactant and the sum of the reactant exponents is two, then the reaction is a second-order reaction. The second-order rate law is given by

$$r = \frac{d[C]}{dt} = k[C]^2$$

With integration of this expression yielding

$$\frac{1}{[C]} = \frac{1}{C_o} + kt$$

Where plotting $\frac{1}{[C]}$ vs. time gives a linear plot with a slope of -k.

In order to define the rate order of a reaction, zero, first, and second order plots vs. time are created using the rate law and the plot with a linear trend determines the order of the rate.

For these experiments, the sample was prepared in the u-tube as previously described and then placed in reactor 1 under inert conditions with a flowrate of 175 ml/min of pure Argon. A TPD was conducted to remove the volatile fraction. The sample was heated to the temperature of interest under inert conditions, then the gas flow was switched to 20% O_2 in Ar for the temperature-specified duration and then switched back for a five minute recovery period in inert conditions. This process was repeatedly cycled until the consumption of the entire sample. The nature of the VI code for the switching valve allows for user selection of O_2 pulse durations, with the CRCL Microreactor capable of durations

between 2s and 180s. The effluent gases were measured with a mass spectrometer, and the CO_2 recorded resulted in the computation of the reaction rate.

CHAPTER III

RESULTS AND DISCUSSION

3.1 Experimental Repeatability

Due to the expensive and arduous nature of acquiring the GDI particulate matter (done at ORNL), the CRCL only has a limited, precious quantity of the sample. This means there was no room for error when performing the experiments needed to characterize and compare the different fuel derived particulate matter samples. Our lab has a rather large inventory of medium-duty diesel (MD-ULSD) particulate matter, which has previously been well characterized; therefore, preliminary and proof-of concept experiments were performed using this [16, 47].

In order to confidently move forward with the experiments on the GDI PM, the procedures and experimental conditions representative of GDI exhaust were validated on medium-duty ultra low sulfur diesel PM. Therefore, three sets of preliminary studies were done to evaluate experiment repeatability, the effect of O_2 concentration, and the effect of flowrate. Figure 10 shows CO_2 concentration versus time curves from repeated TPO experiments on ULSD.

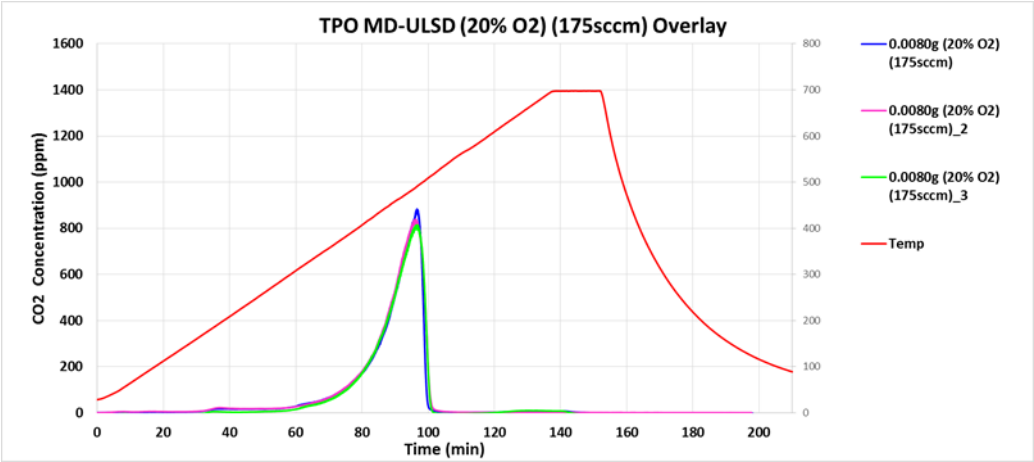

Figure 10: MD ULSD TPO Overlay

The plot shows CO_2 concentration on the left axes, and temperature on the right axes, the x-axis is time, in minutes. At the experimental conditions shown (20% O_2 concentration, 175sccm total flowrate), three different samples of 8mg each were TPO-ed and the results overlaid. The figure shows excellent repeatability in the three CO_2 concentration curves. Physically, at the start of the experiment, due to the low temperature, none of the particulate matter is reacting with the O_2, which is why the baseline for CO_2 stays constant. The reaction begins to light-off around 350°C, indicated by the increase in CO_2 concentration, representing approximately 10% of sample consumption. Shortly after, the concentration escalates swiftly until the CO_2 concentration peaks at roughly 555°C; then rapidly decreases until the starting baseline is achieved again **Table 1** shows the temperature at several burnout percentages from the three experiments in Figure 10 as well as the peak temperature of each sample.

	Sample		
	0.0080g (20% O2)	0.0080g (20% O2) (2nd)	0.0080g (20% O2) (3rd)
Temp_10% (C)	414.9	405.3	423.4
Temp_25% (C)	476.6	468.2	479.3
Temp_50% (C)	516.0	511.6	516.3
Temp_75% (C)	536.6	530.3	534.5
Temp_95% (C)	548.7	543.0	546.3
Temp_Peak (C)	558.9	554.2	552.8

Table 1: MD ULSD TPO Burnout Percentage Temperatures

It can be concluded from the data presented in the table and the identical nature of the curves in the plot, that the experiment is repeatable.

3.2 Effect of O_2 Concentration

One major parameter in TPX experiments is oxygen concentration in the influent gas stream. Previously, since our focus was on diesel particulate, we used 10 vol% O_2 in Argon for the oxidizing condition. However, GDI exhaust contains a higher concentration of O_2 as compared to diesel exhaust. We investigated the effect of O_2 concentration on the bulk reactivity as measured by TPO. .

Five replicates were done at each O_2 concentration. The results can be seen in **Figure 11**, as well as the resultant average data from each concentration in **Table 2**.

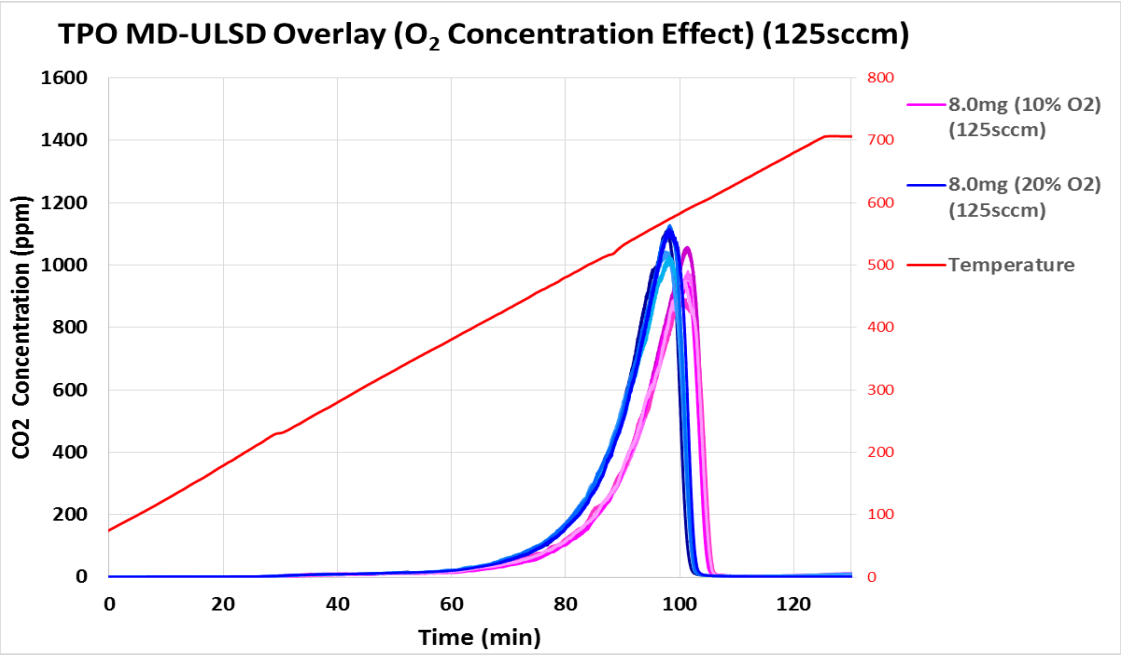

Figure 11: MD ULSD TPO Concentration Effect Overlay

	Sample	
	0.0080g (10% O2) (125sccm) Average	**0.0080g (20% O2) (125sccm) Average**
Temp_10% (C)	474.1	458.7
Temp_25% (C)	524.3	508.6
Temp_50% (C)	557.4	542.3
Temp_75% (C)	576.7	561.8
Temp_95% (C)	589.8	574.3
Temp_Peak (C)	585.3	576.5

Table 2: MD ULSD TPO Concentration Effect Average Burnout Temperatures

Comparing the data from the 10% O_2 concentration to the 20% O_2 concentration, a visible shift in both the graphical and numerical data can be seen. The data shows that

increasing the O_2 concentration to 20% causes the TPO curves to shift forward by roughly 15°C across the entire reaction. This shift suggests that the 10% O_2 condition may be reactant or diffusion limited.

One additional TPO experiment was performed with 30% O_2 in Argon. The results from this experiment were then compared to the previous experiments, and can be seen in **Figure 12** and **Table 3**

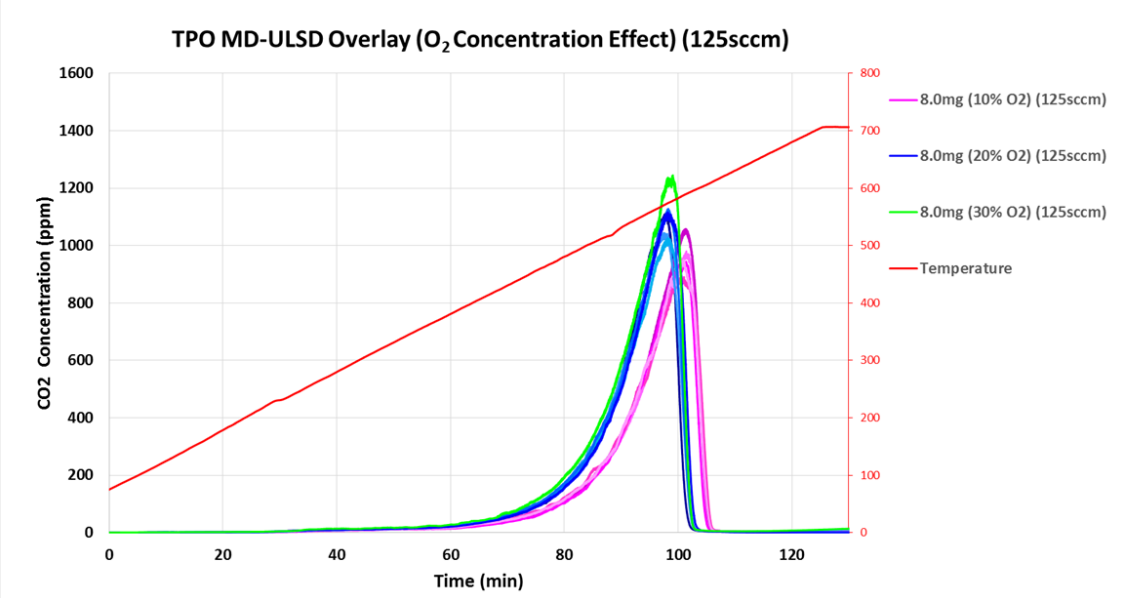

Figure 12: MD ULSD TPO Concentration Effect Overlay

	Sample		
	0.0080g (10% O2) (125sccm) Average	0.0080g (20% O2) (125sccm) Average	0.0080g (30% O2) (125sccm)
Temp_10% (C)	474.1	458.7	449.5
Temp_25% (C)	524.3	508.6	501.9
Temp_50% (C)	557.4	542.3	535.8
Temp_75% (C)	576.7	561.8	556.8
Temp_95% (C)	589.8	574.3	570.7
Temp_Peak (C)	585.3	576.5	574.5

Table 3: MD ULSD TPO Concentration Effect Average Burnout Temperatures

There is no evident shift between the 20% and 30% O_2 conditions, meaning that at 20% O_2 concentration and upward, the experiment is no longer limited.

3.3 Effect of Experimental Flowrate

Previous, diesel-focused TPX experiments in the CRCL have been performed with a total flowrate of 175sccm. GDI exhaust typically has a higher space velocity as compared to diesel, so the effect of flowrate in TPO experiments was examined.

Three flowrates of 125, 175, and 225sccm were examined. **Figure 13** shows the CO_2 concentration versus time plots for TPO experiments for these three different flowrates. **Table 4** shows the temperature data for percentage burned

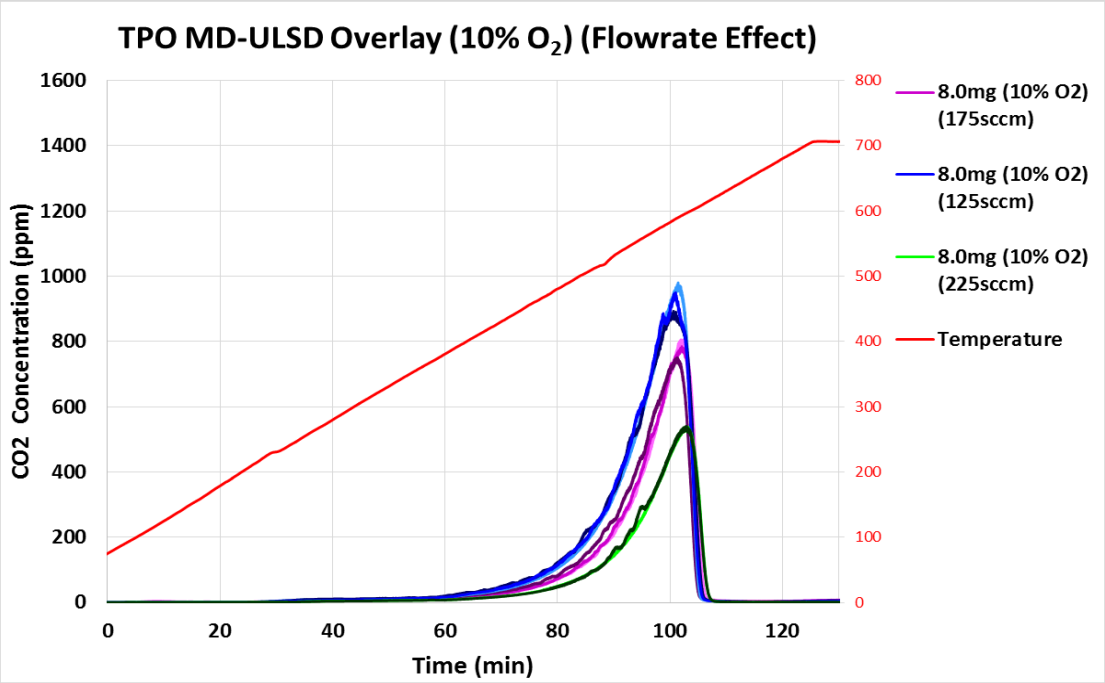

Figure 13: MD ULSD TPO Flowrate Effect Overlay

	Sample		
	0.0080g (10% O2) (125sccm) Average	0.0080g (10% O2) (175sccm) Average	0.0080g (10% O2) (225sccm) Average
Temp_10% (C)	474.1	467.7	478.7
Temp_25% (C)	524.3	522.7	528.7
Temp_50% (C)	557.4	557.3	562.9
Temp_75% (C)	576.7	576.4	583.7
Temp_95% (C)	589.8	588.1	596.2
Temp_Peak (C)	585.3	587.7	590.6

Table 4: MD ULSD TPO Flowrate Effect Average Burnout Temperatures

Comparing the reactivity of the samples exposed to the three different flowrates, it can be seen that increasing the flowrate will shift the TPO curve slightly to higher temperatures (with the max change being 5°C). This effect could be due to increased heat

transfer away from the combusting sample due to the higher flowrate. There is a downward shift in peak concentration as flowrate increases. This is due to the fact that since the flowrate is higher; the total volume is increased, which in turn makes the concentration lower.

3.4 Effect of Water

Tailpipe exhaust from real driving applications contains 5 to 10% water in the exhaust gas mixture. To simulate real world conditions, the CRCL's Microreactor was modified with a water addition system for the influent gas stream to enable us to determine the effect water has on particulate matter reactivity.

In order to incorporate water into the gas stream, a water bath is used to heat up a glass bottle containing liquid water to a selected temperature. The temperature of the water bath psychometrically determines the water concentration that the Argon gas can pick up as it flows through the water bottle. This concentration is calculated from the water vapor pressure curve obtained by plotting Temperature versus Pressure for water. The slope of this curve, seen in **Figure 14**, is used to calculate the concentration of the bottle.

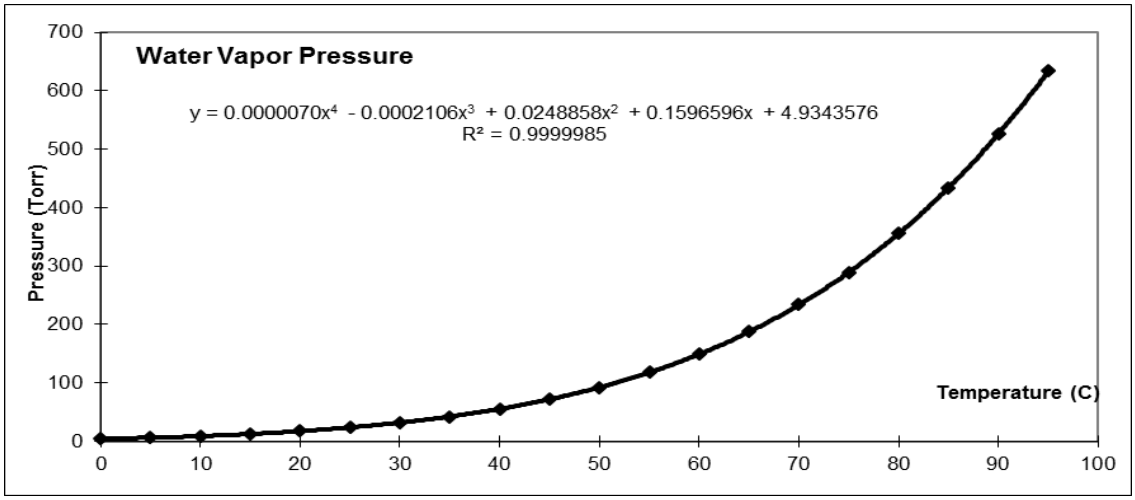

Figure 14: Water Vapor Pressure Curve

The flowrate of Argon passing through the bottle, along with the temperature of the water bath, determines the exact, desired humidity concentration exiting the bottle. After the water/Argon mixture exits the water bottle, it flows into an auxiliary port, which connects with the main gas input line before the sample in Reactor 1. The mixture then mixes further with the other gases (O_2 and Ar) and reacts with the sample.

In order to determine the effect humidity level has on particulate matter reactivity, TPO experiments were performed on ULSD particulate matter with 10% H_2O in the influent gas stream, as well as the new experimental conditions of 20% O_2 concentration with a total gas flow of 175sccm. **Figure 15** compares the CO_2 concentration plot versus time curves for a sample containing 10% H_2O in the input gas steam to one with no H_2O in the gas stream. Temperature data for percentage mass burned can be seen below in **Table 5**

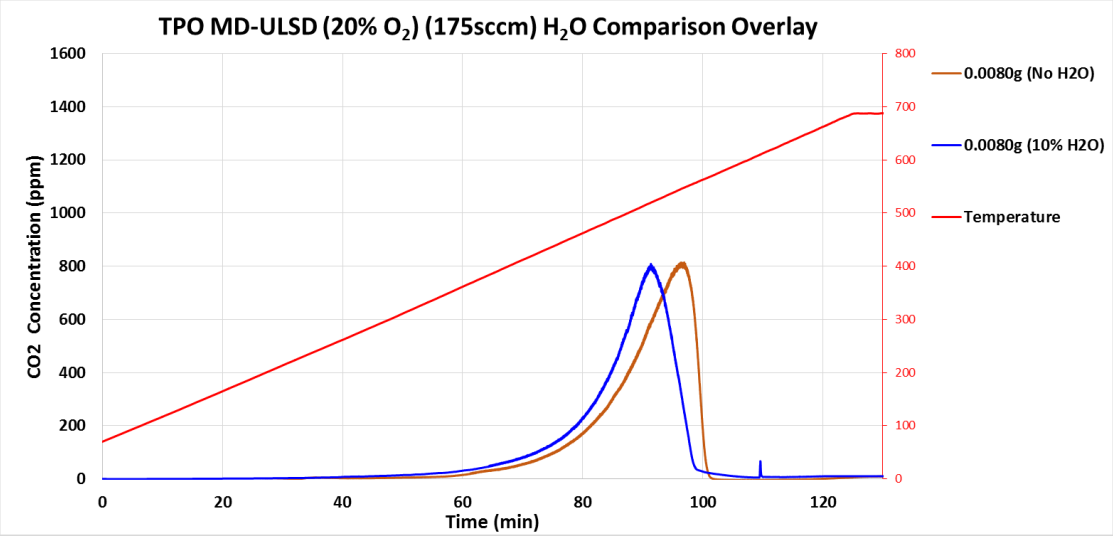

Figure 15: MD ULSD TPO Water Addition Overlay

	Sample	
	0.0080g (No H2O)	0.0080g (10% H2O)
Temp_10% (C)	423.4	401.4
Temp_25% (C)	479.3	451.9
Temp_50% (C)	516.3	485.8
Temp_75% (C)	534.5	504.5
Temp_95% (C)	546.3	516.6
Temp_Peak (C)	552.8	514.5

Table 5: MD ULSD TPO Water Addition Burnout Temperatures

It can clearly be seen that the inclusion of 10% H_2O to the gas stream shifts the TPO curves by 20°C, then increasing amounts across the entire duration of the reaction. This effect suggests that H_2O is behaving as a third body interacter and is catalyzing the reaction through its participation.

3.5 Effect of Fuel Type

3.5.1 BET Surface Area

As previously described in Section 2.2.4, the specific surface area of GDI E0 and E30 particulate samples was measured via BET experiments in the CRCL Microreactor using Argon adsorption isotherms at 77K. For each GDI sample, E0 and E30, an experiment was performed on the nascent PM sample, as well as a devolatilized sample. This allows for a measurement of the specific surface area for both the nascent particulate and the fixed carbon content. In order for BET theory to remain applicable, the measured C value, which describes the difference in heat of adsorption of the first layer and heat of condensation for the remaining layers, must always be positive and not greater than 200 [48]. Also, the resultant BET plot must maintain a positive increase in $V_{ads}(1-P/P^o)$ as a function of relative pressure across the range $0.05< P/P^o<0.3$ [48]. This increase is demonstrated by the R^2 value, taken from the slope of the BET plot, in the subsequent tables. **Table 6**: BET Surface Area Data for nascent GDI E0 PM shows the results from the BET experiments on two nascent GDI E0 PM samples.

Sample	Mass (mg)	Replicate	Specific Surface Area (m^2/g)	R^2 value of fit line	C value	**Average Specific Surface Area (m^2/g)**	std deviation
E0 #1	9.1	1	78	0.9976	10.08	81.75	2.99
		2	83	0.9979	15.06		
		3	81	0.9988	12.67		
		4	85	0.9983	10.93		
E0 #2	10.1	1	82	0.9984	39.24	81.25	0.96
		2	80	0.999	29.62		
		3	82	0.9979	23.09		
		4	81	0.9991	29.6		
					average	**81.5**	2.07

Table 6: BET Surface Area Data for nascent GDI E0 PM samples

Four different BET experiments were performed on each GDI E0 for statistical purposes and an average specific surface area was taken from those results. With all C values remaining positive and an increase in pressure observed with each experiment with R^2 values near 1, BET theory is upheld, with results reported with confidence.

Table 7 shows the results from the BET experiments on a devolatilized GDI E0 PM samples.

Devol Sample	Mass (mg)	Replicate	Total Surface Area (m^2/g)	R^2 value of fit line	C value	**Average total Surface Area (m^2/g)**	std deviation
1	9.3	1	235	0.9994	28.33	**234.75**	3.4
		2	230	0.9998	44.12		
		3	238	0.9982	42.02		
		4	236	0.9998	40.11		

Table 7: BET Surface Area Data for a devolatilized GDI E0 PM sample

It can be seen that the removal of the mobile carbon content allows for a 288% increase in specific surface area for the GDI E0 particulate compared to the nascent sample. **Table 8** and **Table 9** show the results from the BET experiments on two nascent GDI E30 PM samples and one devolatilized GDI E30 PM sample, respectively.

Sample	Mass (mg)	Replicate	Specific Surface Area (m^2/g)	R^2 value of fit line	C value	**Average Specific Surface Area (m^2/g)**	std deviation
E30 #1	9.1	1	103	0.9989	26.6	102	1.83
		2	101	0.9985	36.49		
		3	104	0.9991	16.52		
		4	100	0.9994	20.18		
E30 #2	10.4	1	103	0.9994	40.63	102.5	1.29
		2	104	0.9991	47.01		
		3	101	0.9989	48.74		
		4	102	0.9991	46.44		
					average	**102.25**	1.49

Table 8: BET Surface Area Data for nascent GDI E30 PM samples

Devol Sample	Mass (mg)	Replicate	Total Surface Area (m^2/g)	R^2 value of fit line	C value	**Average total Surface Area (m^2/g)**	std deviation
1	9.4	1	259	0.9996	58.45	**257**	2.31
		2	255	0.9994	54.9		
		3	259	0.9989	57.68		
		4	255	0.9991	52.46		

Table 9: BET Surface Area Data for a devolatilized GDI E30 PM sample

Four different BET experiments were performed on each GDI E30 for statistical purposes and an average was taken from those results. The data shows that removing the

volatile content of the GDI E30 PM increases the specific surface area by 251%, compared to the nascent sample. **Figure 16** shows the average results from the nascent and devolatilized BET experiments for GDI E0 and E30.

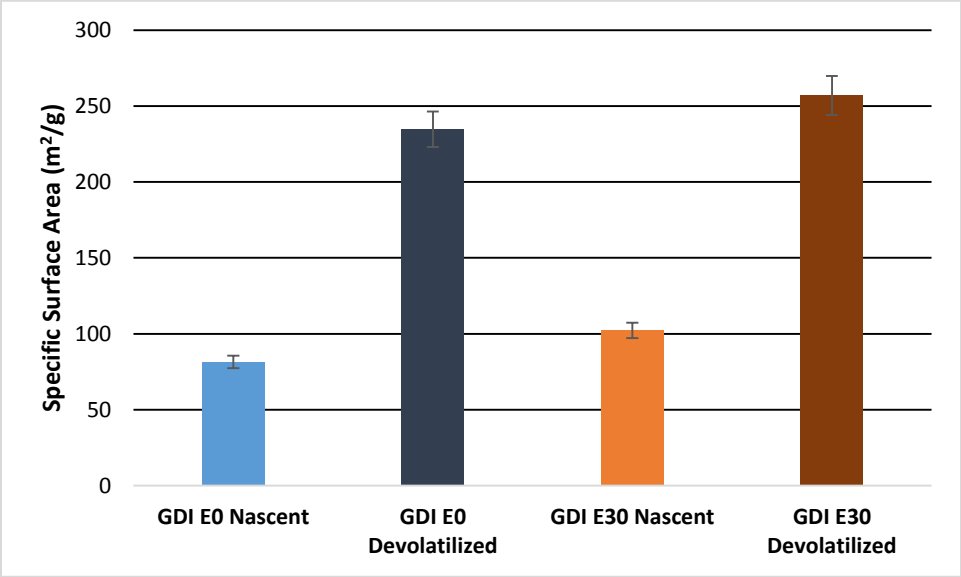

Figure 16: Average Specific Surface Area Values for GDI E0 & E30 PM

It can be seen from the figure, that removal of volatile content in both GDI E0 and E30 PM results in increases in specific surface area of similar value for both samples.

In order to better understand the nature of the solid-gas reactions of the PM, the change in surface area throughout the extent of burnout must be measured. Future work needs to be done in this regard.

3.5.2 Temperature Programmed Oxidation

Temperature Programmed Oxidation (TPO) experiments were performed on the CRCL Microreactor in order to analyze the bulk oxidative behavior of the GDI E0 and

E30 PM samples. MD ULSD PM was also analyzed and compared to the GDI PM, acting as a benchmark due to it being previously studied and readily available in abundant quantities. The results of the nascent TPO's were plotted by CO_2 concentration vs. time for comparison. **Figure 17** shows the TPO curves for GDI E0 and E30 and MD ULSD PM.

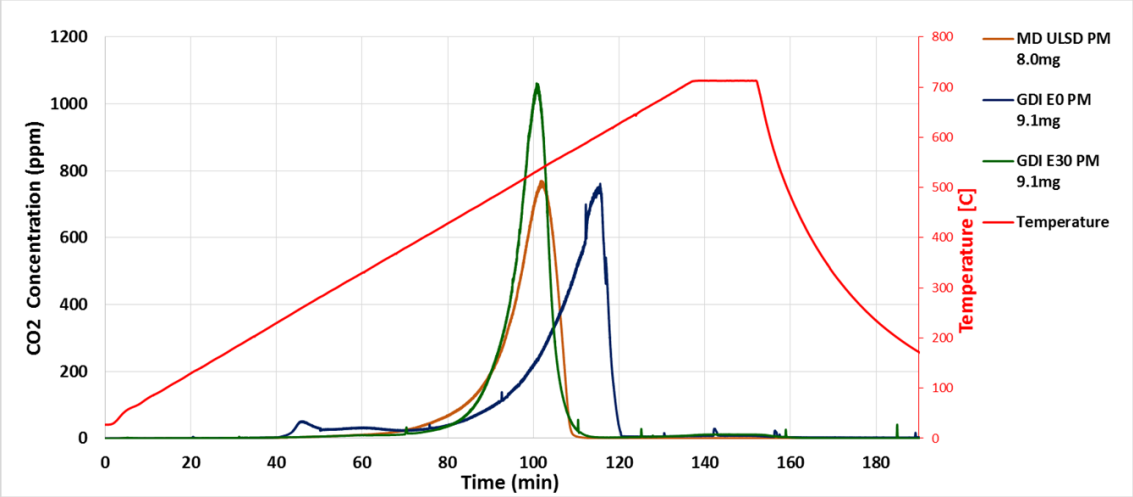

Figure 17: TPO Overlay for GDI E0, GDI E30, and MD ULSD PM

All three experiments consisted of the same experimental conditions, 20% O_2 concentration, 10% H_2O in the influent gas stream, and 175sccm total flowrate. The plot shows CO_2 concentration on the left axes, and temperature on the right axes, the x-axis is time, in minutes. To the left of the graph, the legend is shown for the different PM, along with the respective sample sizes. The temperature curve is shown in red. **Table 10** shows the temperature at several burnout percentages from the three experiments in **Figure 17**, as well as the peak temperature of each sample.

	Sample		
	TPO MD ULSD PM (8.0mg)	**TPO GDI E0 PM (9.1mg)**	**TPO GDI E30 PM (9.1mg)**
Temp_10% (C)	452.0	381.8	461.3
Temp_25% (C)	498.5	499.4	494.1
Temp_50% (C)	530.4	552.9	516.8
Temp_75% (C)	548.2	581.0	529.2
Temp_95% (C)	563.0	596.7	539.8
Temp_Peak (C)	545.7	605.0	528.9

Table 10: TPO Burnout Temperatures for GDI E0 & E30 and MD ULSD PM

From the figure and table, a clear difference can be seen in the CO_2 profiles of each sample. The CO_2 baseline remains constant for all 3 samples at the beginning of the temperature ramp, indicating no carbon reaction with O_2. GDI E0 lights-off first around 380°C, approximately 75°C earlier than the other two samples, but has the highest peak temperature at 605°C. GDI E30 has a similar CO_2 profile to MD ULSD, however, it has a light-off temperature 9°C later than MD ULSD, but a peak temperature approximately 16°C earlier. GDI E30 also has a peak CO_2 concentration nearly 300ppm larger than the other samples. The higher and tighter nature of the GDI E30 peak suggests a more homogenous structure of the carbon lamella which comprise the nanostructure of the PM. This indicates GDI E30 particulates are the most reactive, followed closely by MD

ULSD PM, and with GDI E0 being the least reactive PM. This trend is expected due to the inclusion of 30% ethanol in the fuel the particulate is obtained from.

The fixed carbon and mobile carbon content were examined separately to help determine the reactivity differences of the solid carbon fractions of the PM, which is the portion of interest for GPF behavior.

3.5.3 Temperature Programmed Desorption

In order to quantify the volatile organic fraction (vof), Temperature Programmed Desorption experiments were performed in the CRCL Microreactor on both GDI PM samples, as well as a MD ULSD PM sample. The results of the TPD experiments were plotted by CO_2 concentration vs. time for comparison. **Figure 18** shows the CO_2 concentration versus time plots for TPD experiments for these three different samples.

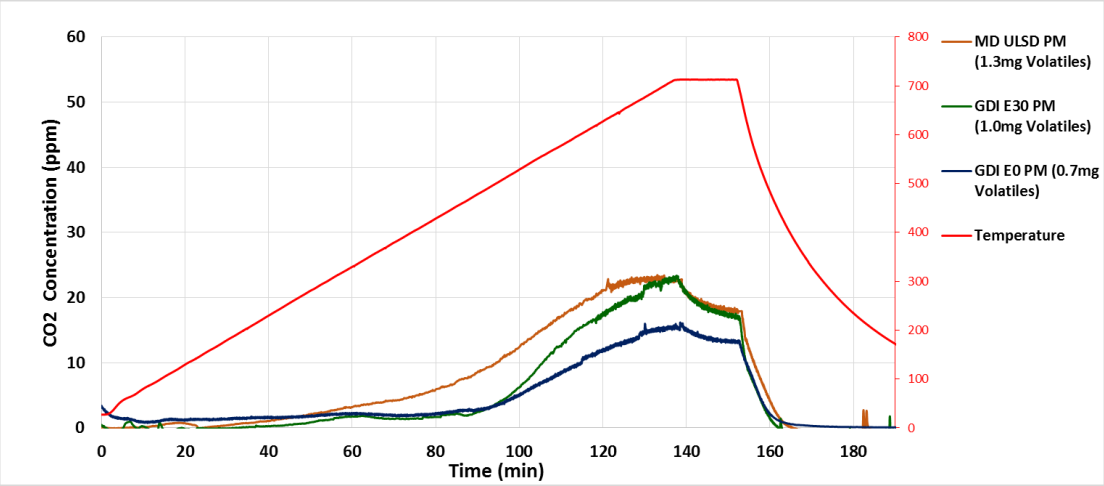

Figure 18: TPD Overlay for GDI E0, GDI E30, and MD ULSD PM

All three experiments consisted of the same experimental conditions, 10% H_2O in the influent gas stream, 175sccm total flowrate, and 20% O_2 concentration in the second reactor cell to oxidize the volatiles. It can be seen that all three samples follow

the same relative trend for their CO_2 concentration curve. MD ULSD PM has more volatiles evaporate off at lower temperatures, while GDI E30 mimics the concentration curve of E0 until increasing to a higher concentration from 525°C onward. It should be noted the CO_2 concentration data in **Figure 18** was passed through a moving data filter in order to clean up the data and remove spikes in the CO_2 concentration caused by water droplets accumulating in the gas stream line sampled by the mass spectrometer. An example of the unfiltered data can be seen in **Appendix B**.

After obtaining the TPD data, the mobile carbon content of the particulate matter samples could be quantified via the volatile organic fraction (VOF). **Figure 19** shows the volatile percent with respect to mass for each sample.

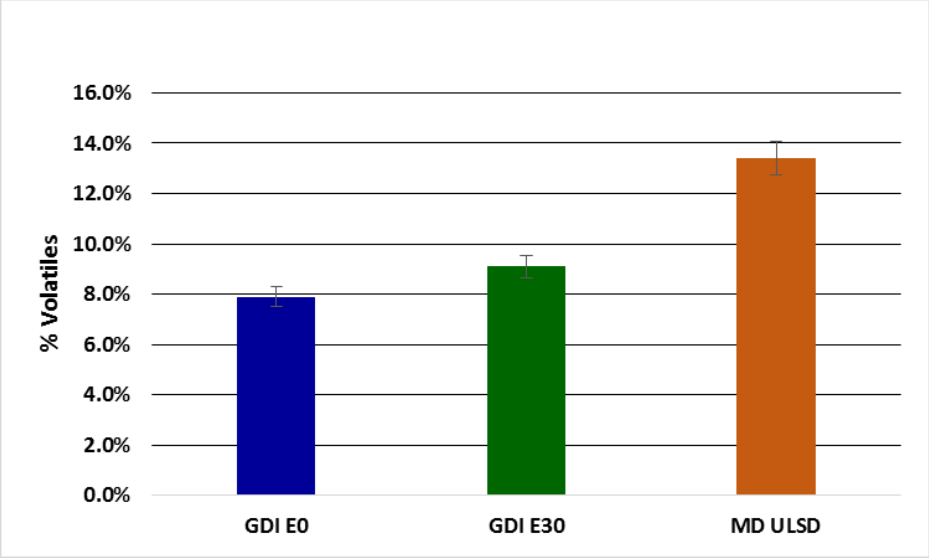

Figure 19: Volatile Carbon Percentages for GDI E0, GDI E30, and MD ULSD PM

This plot shows that the inclusion of ethanol in the fuel causes the amount of mobile carbon in the particulates to increase from 7.9% to 9.1%; however, MD ULSD still has the highest VOF at 13.4%. The increase in mobile carbon content from GDI E0

to E30 is most likely attributed to oxygenates derived from ethanol that are present in the carbon structure, which burnout during TPD. It should be noted that this data shows only a small fraction of the particulates contain mobile carbon, while the majority of the nascent PM is composed of fixed carbon.

3.5.4 Temperature Programmed Oxidation on a Devolatilized Sample

Once the samples have undergone devolatilization via TPD, a TPO was performed on the devolatilized sample in order to quantify the remaining fixed carbon content of the PM. The results of the devolatilized TPO's were plotted by CO_2 concentration vs. time for comparison. **Figure 20** and **Table 11** show the TPO Devol curves and temperature data at several burnout percentages for GDI E0 and E30 and MD ULSD PM. All three experiments consisted of the same experimental conditions, 20% O_2 concentration, 10% H_2O in the influent gas stream, and 175sccm total flowrate.

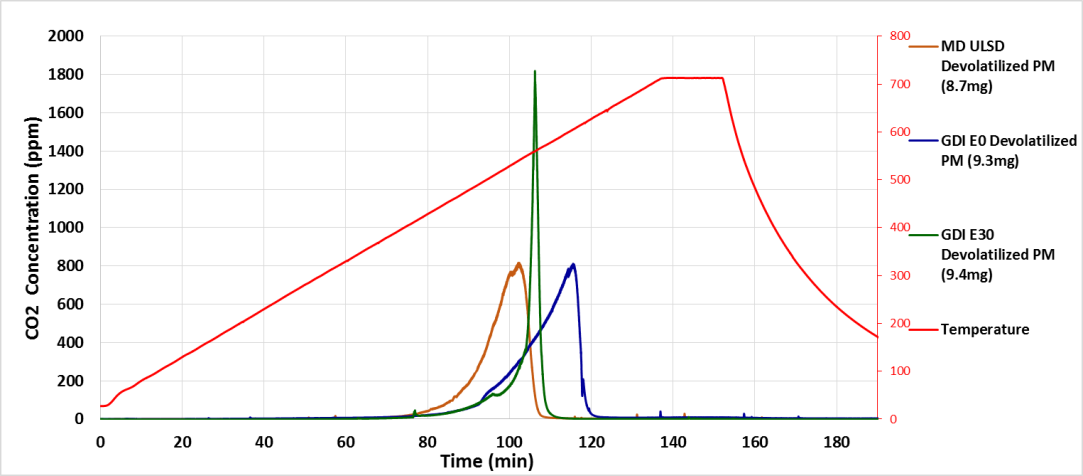

Figure 20: TPO Devolatilized Overlay for GDI E0 & E30 and MD ULSD PM

	Sample		
	TPO Devol MD ULSD PM (8.7mg)	**TPO Devol GDI E0 PM (9.3mg)**	**TPO Devol GDI E30 PM (9.4mg)**
Temp_10% (C)	470.2	499.5	480.7
Temp_25% (C)	502.5	540.7	525.4
Temp_50% (C)	535.2	561.5	552.0
Temp_75% (C)	541.2	583.1	558.2
Temp_95% (C)	553.2	597.0	569.1
Temp_Peak (C)	550.5	599.4	556.8

Table 11: TPO Devol Burnout Temps for GDI E0 & E30 and MD ULSD PM

The data from the plot and table shows the effect volatiles have on the GDI PM samples. While GDI E0 and MD ULSD PM samples both had modest shifts in burnout and peak temperatures, it can be seen that GDI E30 PM had a drastic shift in temperature by over 20°C across the entire burnout range. The narrower curve shape and higher peak concentration should also be noted and further indicates a more homogenous structure for GDI E30. The variance in sample persists even with the removal of the mobile carbon content, indicating ethanol's effect on the reactivity of GDI PM is greater than the volatile content of carbon.

In order to better understand the impact volatiles have on the oxidative reactivity of the GDI PM samples, an overlay plot for each fuel was created with the nascent TPO, mobile carbon, and fixed carbon TPO. **Figure 21** is the TPX overlay plot for GDI E0 PM.

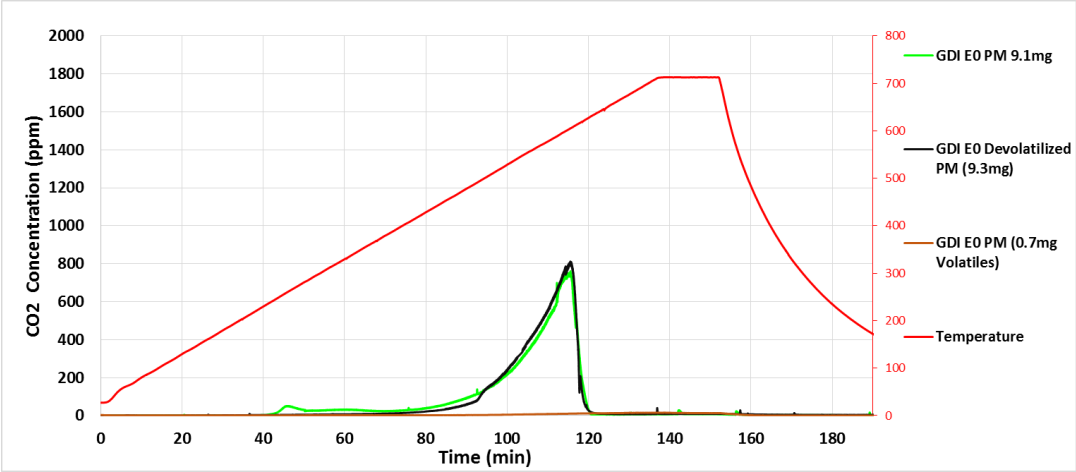

Figure 21: TPX Overlay for GDI E0 PM

This figure shows the removal of only 0.7mg of mobile carbon from GDI E0 PM has a minimal effect on the overall reactivity of the particulate. **Figure 22** shows the TPX overlay plot for GDI E30 PM.

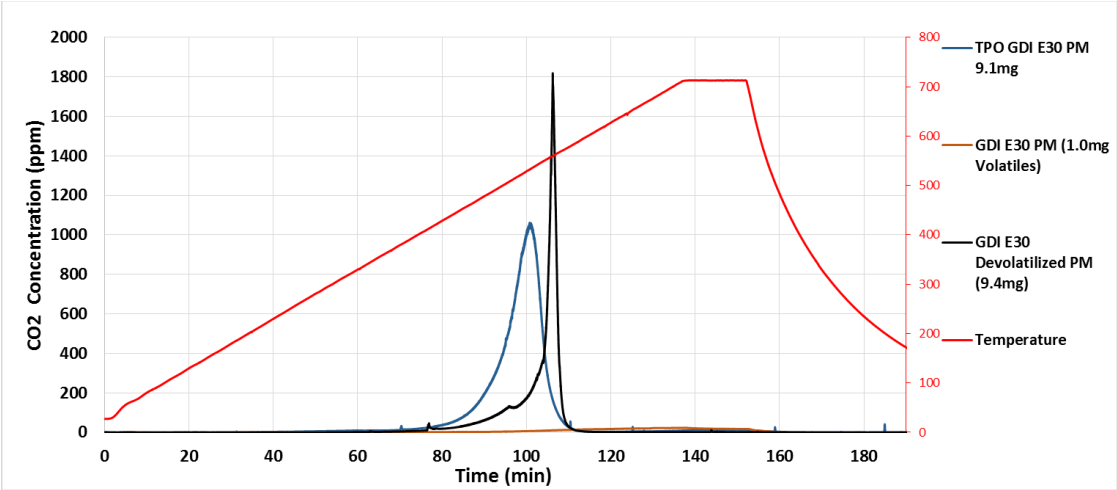

Figure 22: TPX Overlay for GDI E30 PM

It can be seen from the figure that the removal of mobile carbon has a significant effect on the reactivity of GDI E30. The increase in curve shape and peak indicates the

fixed carbon content to be highly reactive in a narrow temperature range. The 20°C shift in temperature across the entire burnout indicates the effect volatile carbon content has at lower temperatures. This suggests fixed carbon is the impetus for the oxidative reactivity of GDI PM. Therefore, measuring the activation energy of the oxidation kinetics will further explain the reactivity process of the PM.

3.5.5 Determination of Reaction Kinetics

Limiting experiments to isothermal, differential measurements lessens the difficulty of calculating kinetic parameters by dissociating the effects of gas parameters. [45] Isothermal Pulsed Oxidation (IPO) experiment were performed in the CRCL Microreator in order to determine the Arrhenius kinetic parameters of GDI E0 & E30 PM. The data obtained from the devolatilized TPO experiments determined the proper temperature range in which to study the GDI particulate samples. For both GDI E0 & E30 samples, the temperatures of 440°C, 490°C, and 510°C were examined. It was verified that each experiment remained differential, less than 5% mass conversion per pulse, throughout the entire duration.

The same experimental conditions were present in all isothermal experiments, minus temperature. The right manifold bank consisted of Argon with 10% H_2O in the influent gas stream with a total flow of 175sccm. The left manifold bank contained 20% O_2 concentration and 10% H_2O in the gas stream, with the remainder being Argon totaling a flowrate of 175sccm. A fast-switching valve was used to switching between banks, with an oxidizing pulse time between 2s and 180s durations, depending on temperature, and an inert recovery period set between 2.5 to 3.5 minutes.

Each particulate sample previous underwent a TPD experiment in order to remove the volatile content, allowing for the experiment to focus solely on the fixed carbon portion of the particulate. A sample mass of 10mg was used for each nascent GDI sample, with devolatilization removing 8% and 9.1% mass for GDI E0 and E30, respectively. **Figure 23**, **Figure 24,** and **Figure 25** are the CO_2 concentration vs. time plots for GDI E0 PM at 440°C, 490°C, and 510°C, respectively.

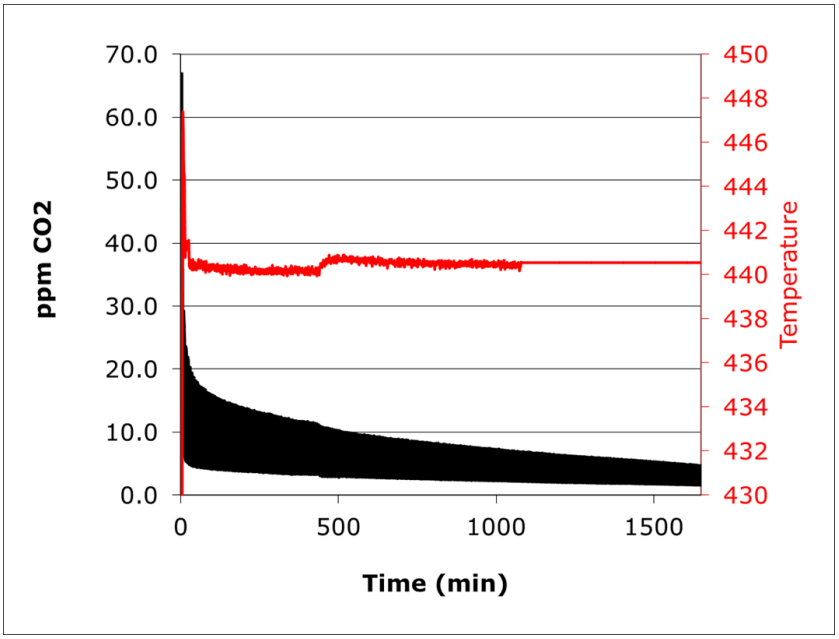

Figure 23: Isothermal Pulsed Oxidation Experiment for GDI E0 PM at 440°C

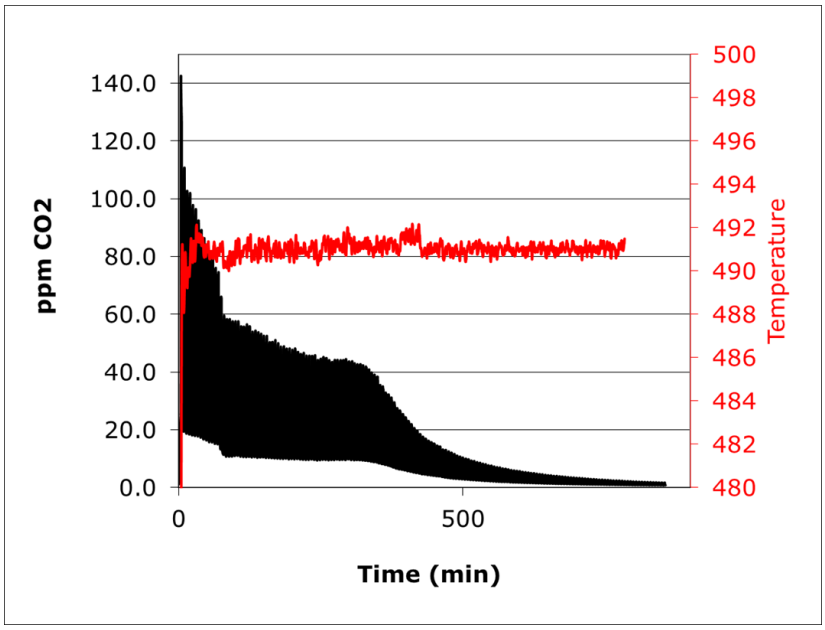

Figure 24: Isothermal Pulsed Oxidation Experiment for GDI E0 PM at 490°C

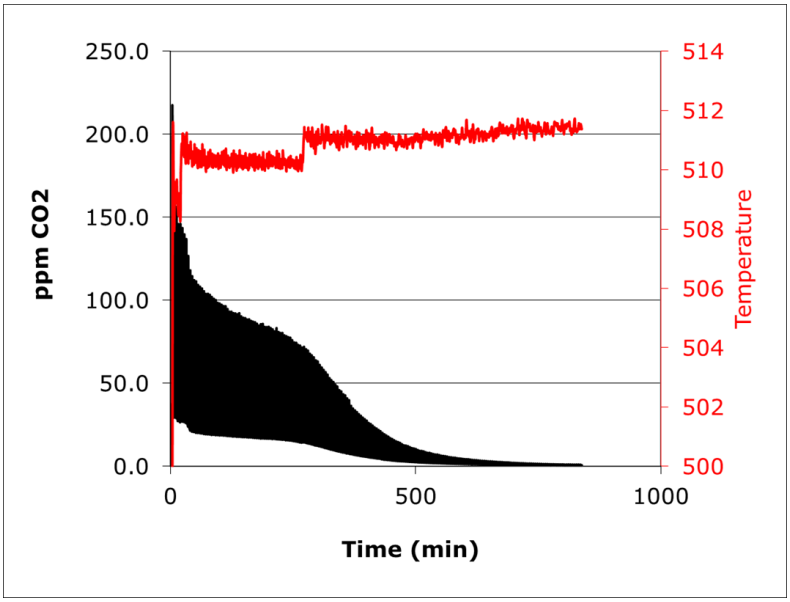

Figure 25: Isothermal Pulsed Oxidation Experiment for GDI E0 PM at 510°C

The plot shows CO_2 concentration on the left axes, and temperature on the right axes, the x-axis is time, in minutes. The temperature curve of the sample bed

temperature is shown in red. The temperature remained within a 1-2°C window, allowing the isothermal assumption to remain applicable.

Figure 26, **Figure 27**, and **Figure 28** are the CO_2 concentration vs. time plots for GDI E30 PM at 440°C, 490°C, and 510°C, respectively.

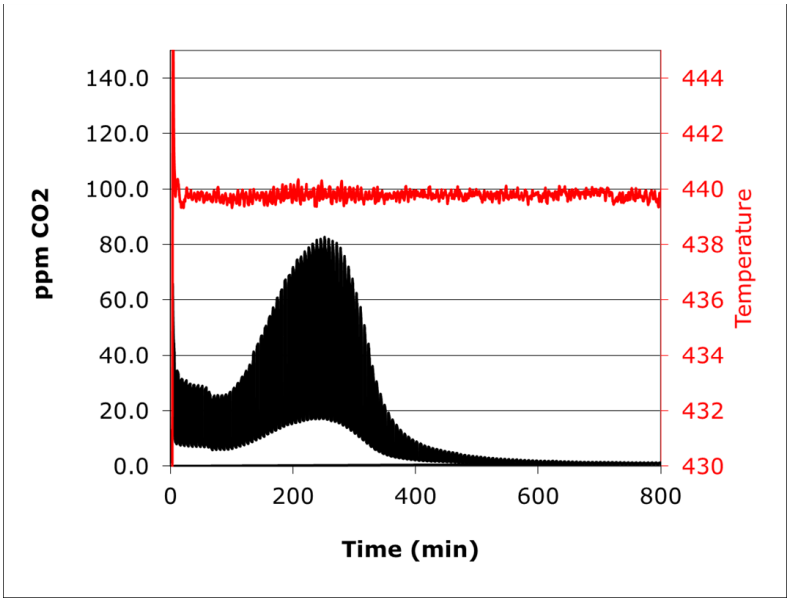

Figure 26: Isothermal Pulsed Oxidation Experiment for GDI E30 PM at 440°C

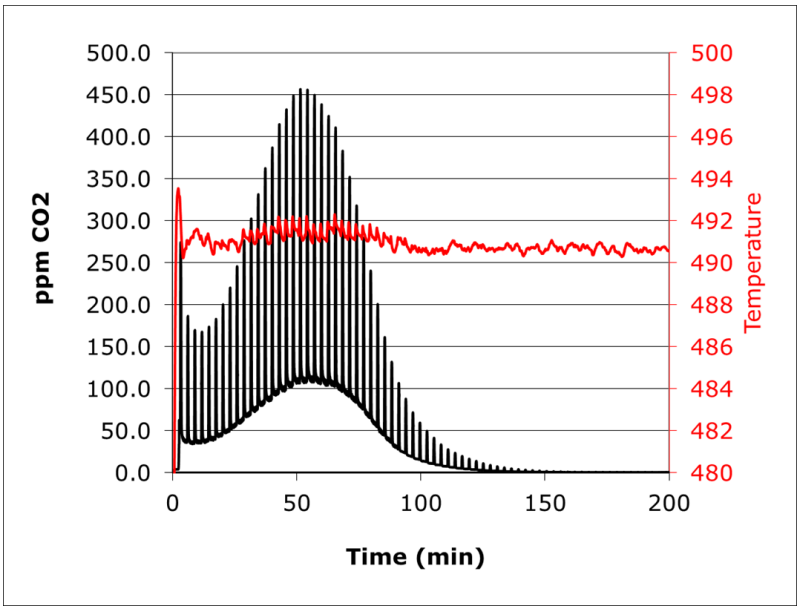

Figure 27: Isothermal Pulsed Oxidation Experiment for GDI E30 PM at 490°C

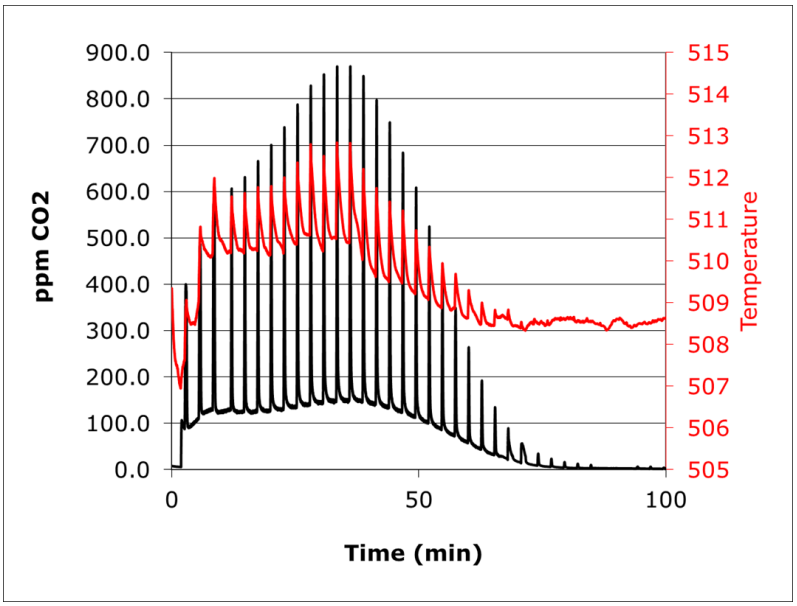

Figure 28: Isothermal Pulsed Oxidation Experiment for GDI E30 PM at 510°C

The temperature remained within a 3-4°C window, allowing the isothermal assumption to remain applicable.

Zero, first, and second order plots were created using the rate law for each pulsing experiment in order to determine the reaction rate order. **Figure 29**, **Figure 30**, and **Figure 31** show the zero, first, and second order plots vs. time, respectively, for the GDI E0 PM pulsing experiment at 490°C.

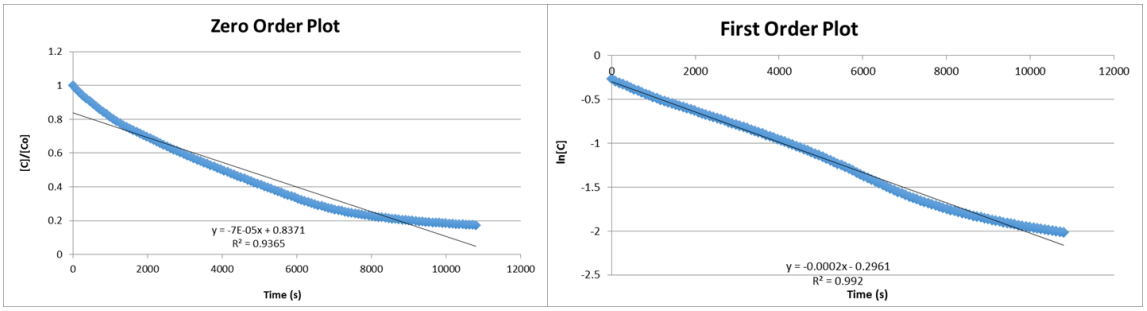

Figure 29: Zero Order Plot from IPO Experiment on GDI E0 PM at 490°C (Left)
Figure 30: First Order Plot from IPO Experiment on GDI E0 PM at 490°C (Right)

Figure 31: Second Order Plot from IPO Experiment on GDI E0 PM at 490°C

From the three plots, a clear linear trend can be seen in the first-order plot for this experiment. Additionally, similar linearity is observed in the first order plots for the GDI E0 PM samples pulsed at 440°C and 510°C, seen in Appendix C, indicating that GDI E0 PM is a first order reaction. As previously discussed, the rate equation to be used is

$$r = \frac{d[C]}{dt} = k[C]^1$$

Figure 32 show that each isothermal pulsing experiment for GDI E0 PM is linear in the first order reaction plot. The effective rate constant for each experiment, k, is calculated from the slope of each line is the plot.

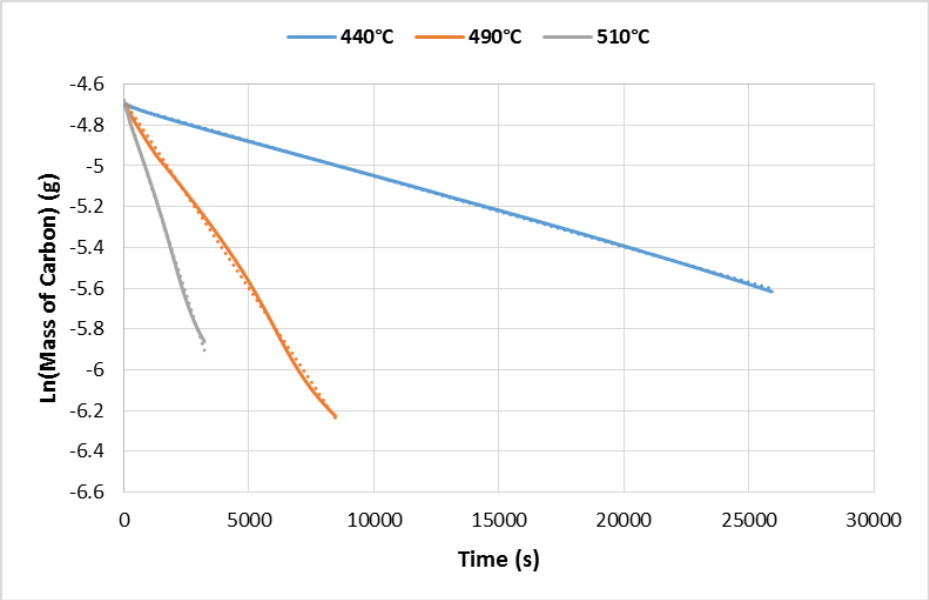

Figure 32: First Order Plot for GDI E0 PM at 3 Different Temperatures

Figure 33,

Figure 34, and **Figure 35** show the zero, first, and second order plots vs. time, respectively, for the GDI E30 PM pulsing experiment at 490°C.

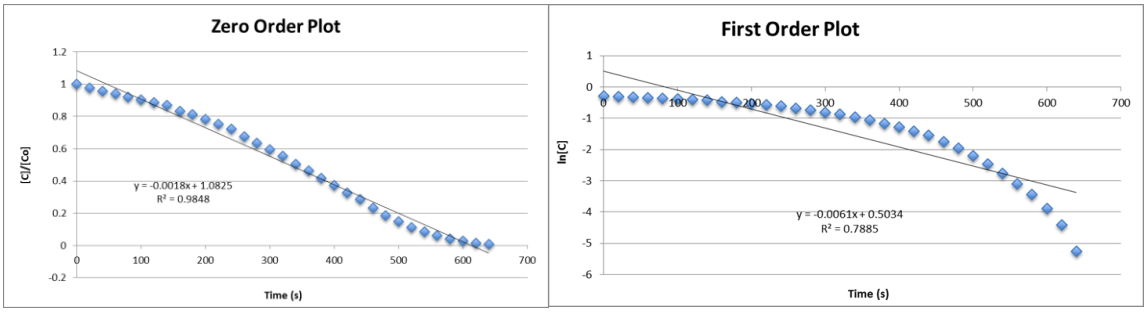

Figure 33: Zero Order Plot from IPO Experiment on GDI E30 PM at 490°C (Left)
Figure 34: First Order Plot from IPO Experiment on GDI E30 PM at 490°C (Right)

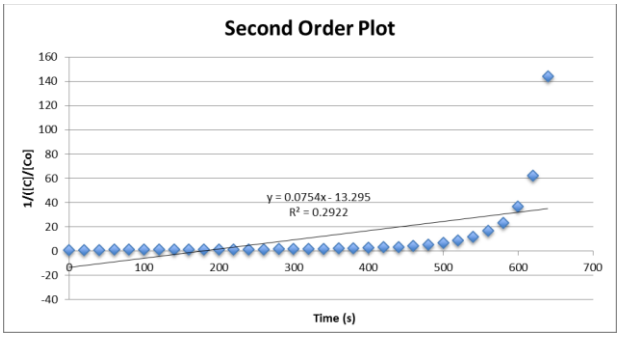

Figure 35: Second Order Plot from IPO Experiment on GDI E30 PM at 490°C

It can be seen from the plots, that linearity is observed in the zero order plot. This is further supported by the plots for the GDI E30 PM experiments at 440°C and 510°C, seen in Appendix D. These trends suggest that GDI E30 particulate is a zero-order reaction, independent of the reactant concentrations. This is a clear difference from the first order reaction rate observed in GDI E0 PM. The reaction rate for a zero order equation is given by

$$r = -\frac{d[C]}{dt} = k[C]^0 = k = constant$$

Figure 36 is the zero-order plot of concentration vs. time for all three isothermal GDI E30 pulsing experiments and confirms a zero-order reaction for GDI E30. The

effective rate constant for each experiment, k, is calculated from the slope of each line is the plot.

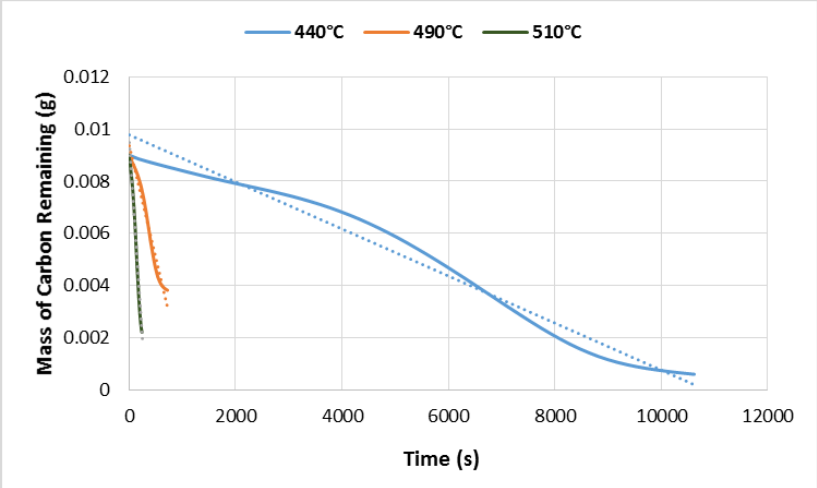

Figure 36: Zero Order Plot for GDI E30 PM at 3 Different Temperatures

The slopes from the GDI E0 first-order plot and the GDI E30 zero-order plot were used to create the reaction rate plots vs. temperature, seen in **Figure 37**.

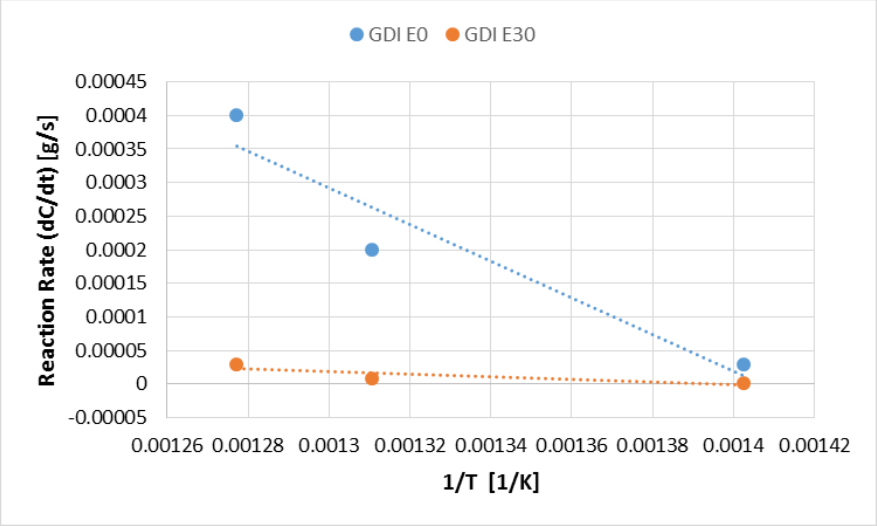

Figure 37: Reaction Rate Plot for GDI E0 and GDI E30

The Arrhenius equation is used to describe the dependence on temperature of the effective reaction rate constants and is given by

$$k = Ae^{(E_A/RT)}$$

with E_A being the activation energy [j/mol], R is the universal gas constant, T is the temperature in Kelvin, and A is the pre-exponential factor. Rearranging the Arrhenius equation gives,

$$\ln(k) = \frac{-E_A}{R}\left(\frac{1}{T}\right) + \ln(A)$$

The Arrhenius plot, plotting $\ln(k)$ vs. $\left(\frac{1}{T}\right)$, allows for the calculation of the activation energy from the slope of the line for each particulate sample and is shown in **Figure 38**.

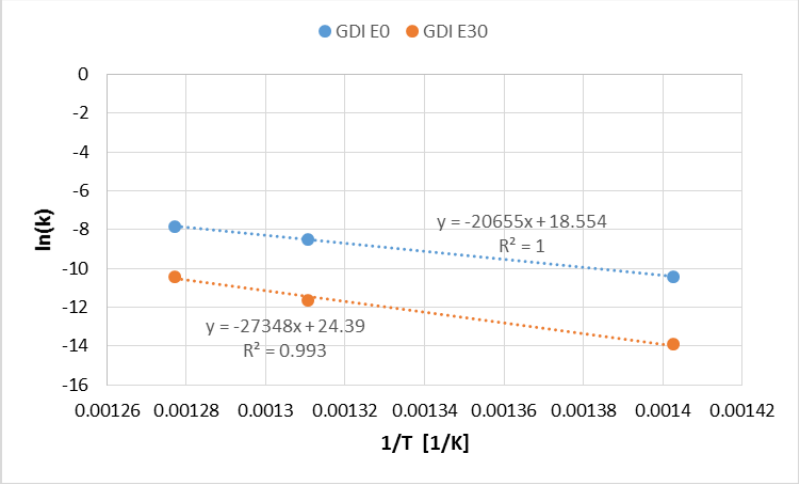

Figure 38: Arrhenius Plot for GDI E0 and GDI E30

From the plot, it can be calculated that the activation energy for GDI E0 PM is 171.7 kJ/mol and the activation energy for GDI E30 PM is 227.4 kJ/mol.

The noted difference in the activation energies, as well as the reaction order rates for the different particulates necessitates the need for further study. It is recommended at least two additional temperatures be examined for isothermal pulsed oxidation experiments for each PM type. It should also be noted that for a solid-gas reaction, the specific surface area of the solid is an important parameter, as previously shown. The need to examine the change in surface area throughout the extent of burnout is clear.

CHAPTER IV

CONCLUSIONS

4.1 Summary

The objective of this study was to examine the effect ethanol has on the reaction kinetics of two different GDI particulates. Initially, preliminary data was taken on MD ULSD PM to verify experiment repeatability and to determine the effects O_2 concentration, flowrate, and the addition of water have on experiments. Then the effect of fuel type was investigated by studying the bulk oxidative reactivity and quantifying the volatile organic fraction and fixed carbon content. It was determined that GDI E30 PM has a higher volatile content than GDI E0 PM and reacts in a narrower band, indicating a homogenous structure. Isothermal-pulsed experiments determined the activation energies to be 171.7 kJ/mol and 227.4 kJ/mol for GDI E0 PM and GDI E30 PM, respectively. BET surface area measurements were performed on nascent and devolatilized samples to determine the specific surface area and the increase that occurs in it with devolatilization.

4.2 Conclusions

The variance observed in activation energies and the reaction order rates of GDI E0 and E30 particulate, indicates that ethanol has an effect of the way GDI PM is formed. Even if oxygenates are present in the particulate structure of GDI E0 or E30 PM, they are removed, along with volatiles, through TPD experiments. This means that both particulate samples consist of amorphous carbon with a fixed carbon content. Therefore, any differences in activation energies or reaction rates must come from physical differences in the carbon nanostructure. The narrow reaction band of GDI E30 along with the reaction

rate being independent of the reaction concentration, suggests that GDI E30 PM is composed of short carbon lamella, which react quickly in the presence of an oxidizer.

4.3 Future Work

Naturally the next step in this work would be to perform additional Isothermal Pulsed Oxidation experiments at different temperatures. For statistical purposes, five total temperatures per sample type would be ideal. This would allow for a more precise calculation of the activation energies.

The difference in activation energies indicates a structural difference in the particulate; therefore, the change in surface area throughout the extent of burnout needs to be examined to determine the effect it poses on the reaction. Ideally, Transmission electron microscopy (TEM) could verify the physical difference and a better understanding of the carbon nanostructures could be attained.

REFERENCES

1. Weinmayr, G., et al., *Long-term exposure to fine particulate matter and incidence of type 2 diabetes mellitus in a cohort study: effects of total and traffic-specific air pollution.* Environmental Health, 2015. **14**(1): p. 53.
2. Hoek, G., et al., *Long-term air pollution exposure and cardio- respiratory mortality: a review.* Environmental Health, 2013. **12**(1): p. 43.
3. Wright, J. and Y. Ding, *Pathophysiological effects of particulate matter air pollution on the central nervous system.* Environmental Disease, 2016. **1**(3): p. 85-89.
4. Anderson, J.O., J.G. Thundiyil, and A. Stolbach, *Clearing the Air: A Review of the Effects of Particulate Matter Air Pollution on Human Health.* Journal of Medical Toxicology, 2012. **8**(2): p. 166-175.
5. Maricq, M., *Gasoline Engines: Ultrafine Particle Emissions.* Physical & Environmental Sciences, Research & Innovation Center, Ford Motor Company. [PowerPoint slides], 2016.
6. Kittelson, D.B., *Engines and nanoparticles: a review.* Journal of Aerosol Science, 1998. **29**(5–6): p. 575-588.
7. Allansson, R., et al., *Optimising the Low Temperature Performance and Regeneration Efficiency of the Continuously Regenerating Diesel Particulate Filter (CR-DPF) System*. 2002, SAE International.

8. Bonatesta, F., E. Chiappetta, and A. La Rocca, *Part-load particulate matter from a GDI engine and the connection with combustion characteristics.* Applied Energy, 2014. **124**: p. 366-376.

9. Daemme, L.C., et al., *Particulate Matter Emissions from a Flexfuel Gasoline Direct Injection Vehicle*. 2015, SAE International.

10. Khalek, I.A., T. Bougher, and J.J. Jetter, *Particle Emissions from a 2009 Gasoline Direct Injection Engine Using Different Commercially Available Fuels.* SAE Int. J. Fuels Lubr., 2010. **3**(2): p. 623-637.

11. Hedge, M., et al., *Effect of EGR on Particle Emissions from a GDI Engine.* SAE Int. J. Engines, 2011. **4**(1): p. 650-666.

12. Chan, T.W., et al., *Evaluation of a Gasoline Particulate Filter to Reduce Particle Emissions from a Gasoline Direct Injection Vehicle.* SAE Int. J. Fuels Lubr., 2012. **5**(3): p. 1277-1290.

13. Richter, J.M., et al., *Application of Catalyzed Gasoline Particulate Filters to GDI Vehicles.* SAE Int. J. Engines, 2012. **5**(3): p. 1361-1370.

14. Parks, J.E., et al., *Filter-based control of particulate matter from a lean gasoline direct injection engine*. 2016, SAE International.

15. Piock, W., et al., *Strategies Towards Meeting Future Particulate Matter Emission Requirements in Homogeneous Gasoline Direct Injection Engines.* 2011.

16. Strzelec, A., *Kinetic model development for the combustion of particulate matter from conventional and soy methyl ester diesel fuels*. Dissertation, University of Wisconsin-Madison, Madison, WI, 2009.

17. Storey, J.M.E., et al., *Exhaust Particle Characterization for Lean and Stoichiometric DI Vehicles Operating on Ethanol-Gasoline Blends*. 2012, SAE International.

18. IEA, *Key World Energy Statistics 2016*. IEA.

19. Apte, J.S., et al., *Addressing Global Mortality from Ambient PM2.5.* Environmental Science & Technology, 2015. **49**(13): p. 8057-8066.

20. Lu, F., et al., *Systematic review and meta-analysis of the adverse health effects of ambient PM2.5 and PM10 pollution in the Chinese population.* Environmental Research, 2015. **136**: p. 196-204.

21. Mamakos, A., et al., *Assessment of different technical options in reducing particle emissions from gasoline direct injection vehicles.* Journal of Aerosol Science, 2013. **63**: p. 115-125.

22. Federal Register / Vol. 79, N.M., April 28, 2014 / Rules and Regulations, http://www.epa.gov/otaq/tier3.htm.

23. Brenzy, R., *Vehicle Emission Standards and Emission Control Experience.* Manufacturers of Emissions Controls Association (MECA). [PowerPoint slides]. 2017.

24. National Highway Traffic Safety Administration., *"2017-2025 Model Year Light-Duty Vehicle GHG Emissions and CAFE Standards: Supplemental" (PDF).*

25. "Draft Technical Assessment Report:Midterm Evaluation of Light-Duty Vehicle Greenhouse Gas Emission Standards and Corporate Average Fuel Economy Standards for Model Years 2022-2025" (PDF).

26. McCormick, R.L., et al., *Bioblendstocks that Enable High Efficiency Engine Designs.* [PowerPoint slides]. 2016.

27. Bandel, W., et al., *The Turbocharged GDI Engine: Boosted Synergies for High Fuel Economy Plus Ultra-low Emission*. 2006, SAE International.

28. Kulzer, A., et al., *Multi-Mode Combustion Strategies with CAI for a GDI Engine*. 2007, SAE International.

29. Maricq, M.M., et al., *Vehicle Exhaust Particle Size Distributions: A Comparison of Tailpipe and Dilution Tunnel Measurements*. 1999, SAE International.

30. Stanglmaier, R.H., J. Li, and R.D. Matthews, *The Effect of In-Cylinder Wall Wetting Location on the HC Emissions from SI Engines*. 1999, SAE International.

31. Stojkovic, B.D., et al., *High-speed imaging of OH* and soot temperature and concentration in a stratified-charge direct-injection gasoline engine.* Proceedings of the Combustion Institute, 2005. **30**(2): p. 2657-2665.

32. Velji, A., et al., *Investigations of the Formation and Oxidation of Soot Inside a Direct Injection Spark Ignition Engine Using Advanced Laser-Techniques*. 2010, SAE International.

33. Li, J., et al., *Liquid Fuel Impingement on In-Cylinder Surfaces as a Source of Hydrocarbon Emissions From Direct Injection Gasoline Engines.* Journal of Engineering for Gas Turbines and Power, 2000. **123**(3): p. 659-668.

34. Su, J., et al., *Particulate Matter Emission Comparison of Spark Ignition Direct Injection (SIDI) and Port Fuel Injection (PFI) Operation of a Boosted Gasoline Engine.* Journal of Engineering for Gas Turbines and Power, 2014. **136**(9): p. 091513-091513-6.

35. Harris, S.J. and M.M. Maricq, *Signature size distributions for diesel and gasoline engine exhaust particulate matter.* Journal of Aerosol Science, 2001. **32**(6): p. 749-764.

36. Bergmann, M., et al., *On-road and laboratory investigation of low-level PM emissions of a modern diesel particulate filter equipped diesel passenger car.* Atmospheric Environment, 2009. **43**(11): p. 1908-1916.

37. Mathis, U., M. Mohr, and A.-M. Forss, *Comprehensive particle characterization of modern gasoline and diesel passenger cars at low ambient temperatures.* Atmospheric Environment, 2005. **39**(1): p. 107-117.

38. Choi, K., et al., *Size-resolved engine exhaust aerosol characteristics in a metal foam particulate filter for GDI light-duty vehicle.* Journal of Aerosol Science, 2013. **57**: p. 1-13.

39. United States. Cong Senate., *Energy Independence and Security Act of 2007. 110th Cong. 1st sess. Public Law 110-140. Washington: GPO 2007. Proquest Congressional Publications. Web.*

40. *Renewable Fuel Standard Program.* . EPA. Environmental Protection Agency, n.d. Web.

41. West, B.H., et al., *Intermediate Ethanol Blends Catalyst Durability Program*. 2012, ; Oak Ridge National Laboratory (ORNL), Oak Ridge, TN (United States). p. Medium: ED.

42. Thompson, T., *Characterization of Remediation Methods for Heavy Hydrocarbon Contaminated Soil*. 2016, Texas A&M University; Combustion and Reaction Characterization Laboratory (CRCL)

43. Lobos, B., *The Use of BET experiments to validate the accuracy and replicability of a microreactor at the Department of Mechanical Engineering, Texas A&M University, Combustion & Reaction Characterization Lab*. Texas A&M University, College Station, TX, 2015.

44. Brunauer, S., P.H. Emmett, and E. Teller, *Adsorption of Gases in Multimolecular Layers.* Journal of the American Chemical Society, 1938. **60**(2): p. 309-319.

45. Yezerets, A., et al., *Differential kinetic analysis of diesel particulate matter (soot) oxidation by oxygen using a step–response technique.* Applied Catalysis B: Environmental, 2005. **61**(1–2): p. 120-129.

46. Strzelec, A., T.J. Toops, and C.S. Daw, *Oxygen Reactivity of Devolatilized Diesel Engine Particulates from Conventional and Biodiesel Fuels.* Energy & Fuels, 2013. **27**(7): p. 3944-3951.

47. Vander Wal, R.L., et al., *Forensics of soot: C5-related nanostructure as a diagnostic of in-cylinder chemistry.* Fuel, 2013. **113**: p. 522-526.

48. Hammond, K.D. and W.C. Conner, *Analysis of Catalyst Surface Structure by Physical Sorption.* Advances in Catalysis, 2013. **56**: p. 1-101.

APPENDIX A

CO_2 CALIBRATION DATA

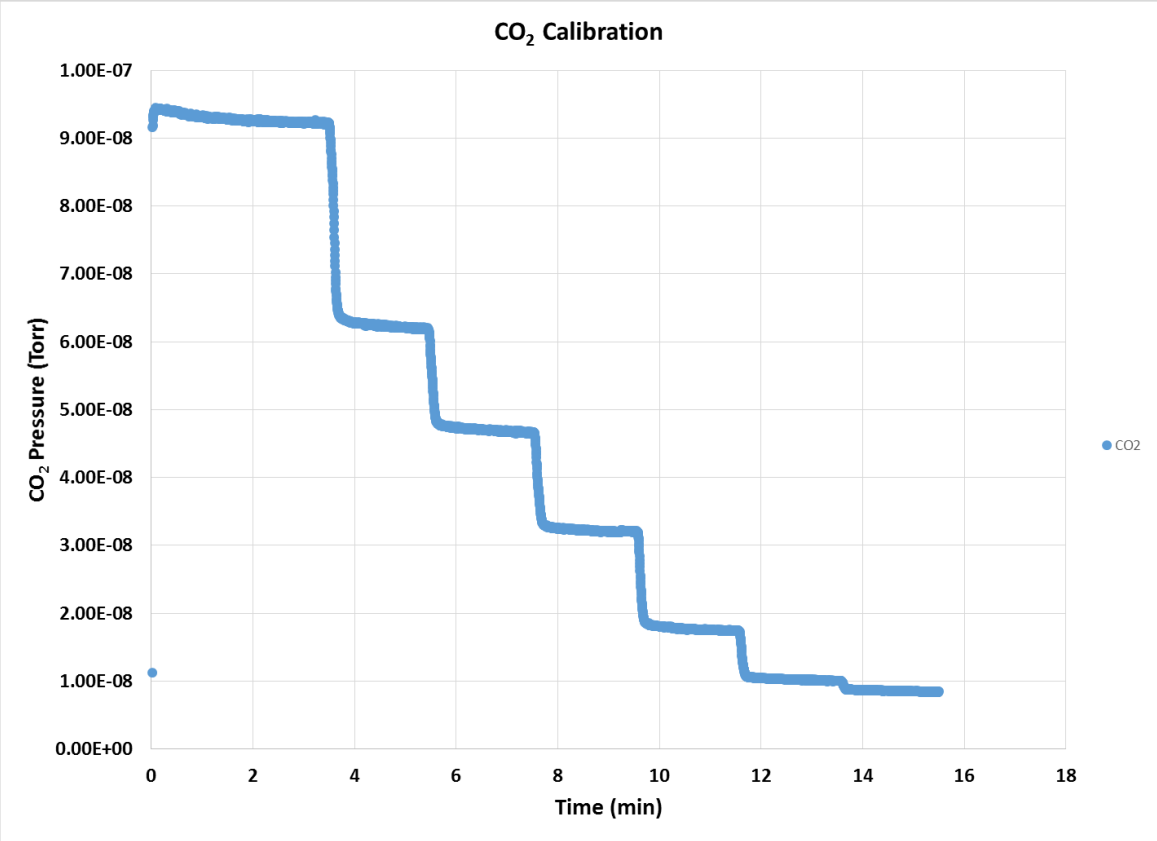

Figure 39: Example of a CO_2 Calibration for the CRCL Microreactor

APPENDIX B

UNFILTERED TEMPERATURE PROGRAMMED DESORPTION DATA

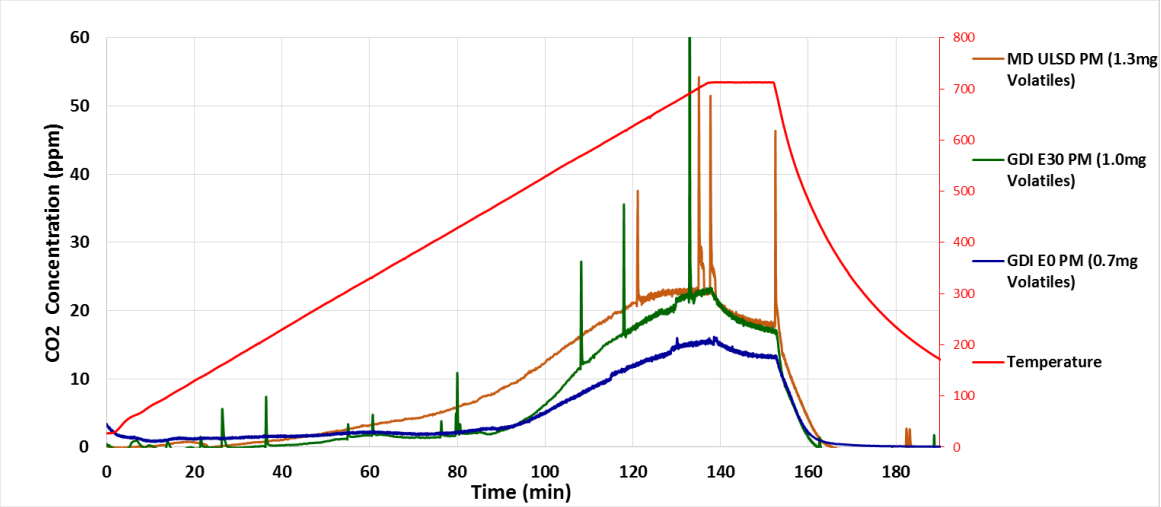

Figure 40: TPD Data before the pressure spikes from the water droplets are filtered

APPENDIX C

REACTION RATE ORDER PLOTS FOR GDI E0 AT 440°C

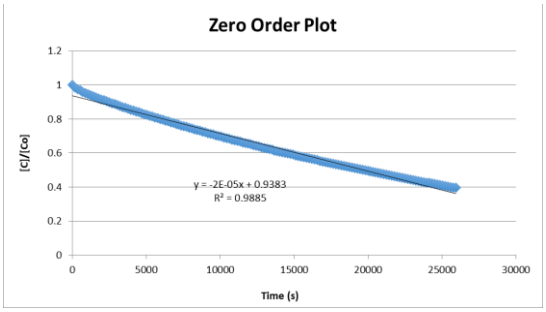

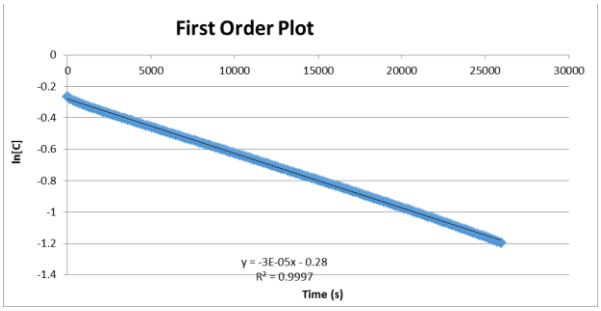

Figure 41: Zero Order Plot from IPO Experiment on GDI E0 PM at 440°C (Left)
Figure 42: First Order Plot from IPO Experiment on GDI E0 PM at 440°C (Right)

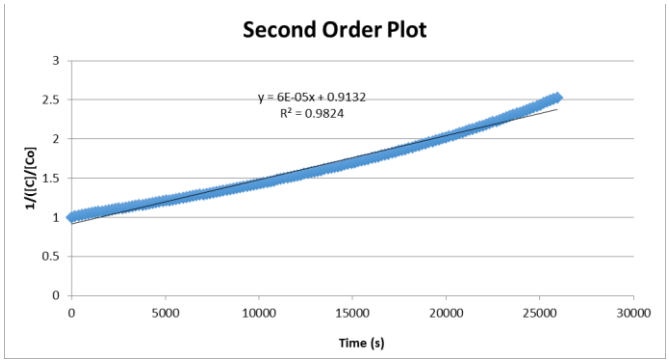

Figure 43: Second Order Plot from IPO Experiment on GDI E0 PM at 440°C (Left)

APPENDIX D

REACTION RATE ORDER PLOTS FOR GDI E0 AT 510°C

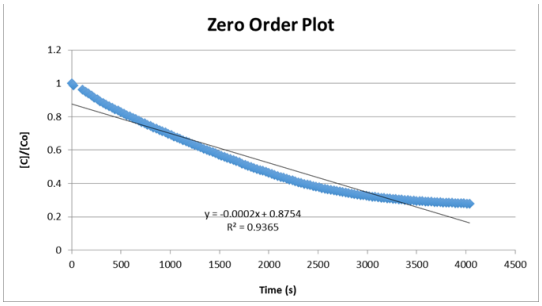

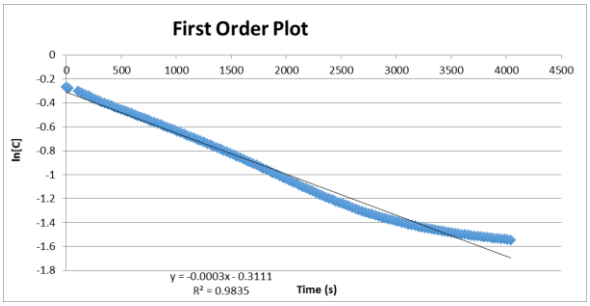

Figure 44: Zero Order Plot from IPO Experiment on GDI E0 PM at 510°C (Left)
Figure 45: First Order Plot from IPO Experiment on GDI E0 PM at 510°C (Right)

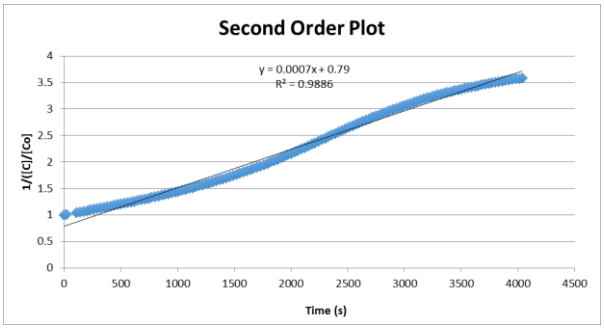

Figure 46: Second Order Plot from IPO Experiment on GDI E0 PM at 510°C

APPENDIX E

REACTION RATE ORDER PLOTS FOR GDI E30 AT 440°C

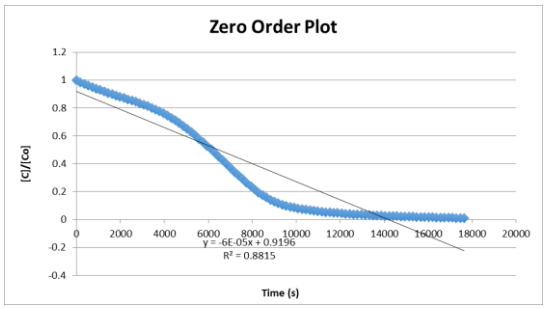

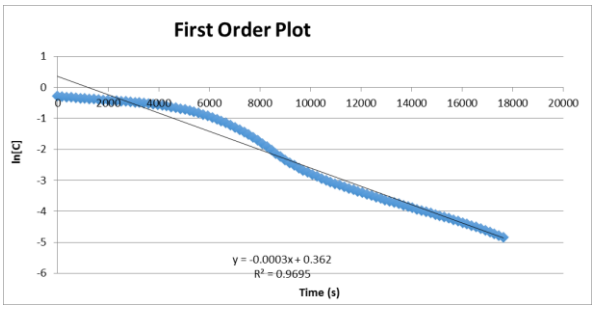

Figure 47: Zero Order Plot from IPO Experiment on GDI E30 PM at 440°C (Left)
Figure 48: First Order Plot from IPO Experiment on GDI E30 PM at 440°C (Right)

Figure 49: Second Order Plot from IPO Experiment on GDI E30 PM at 440°C

APPENDIX F

REACTION RATE ORDER PLOTS FOR GDI E30 AT 510°C

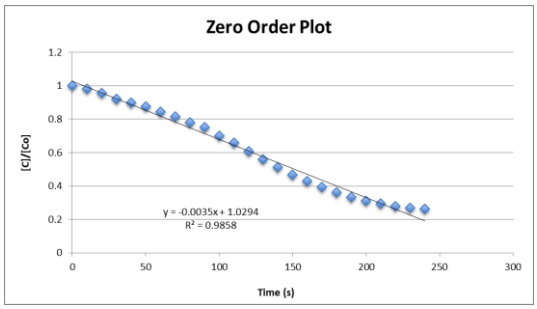

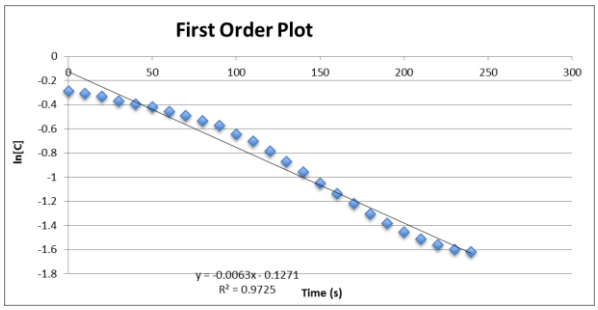

Figure 50: Zero Order Plot from IPO Experiment on GDI E30 PM at 510°C (Left)
Figure 51: First Order Plot from IPO Experiment on GDI E30 PM at 510°C (Right)

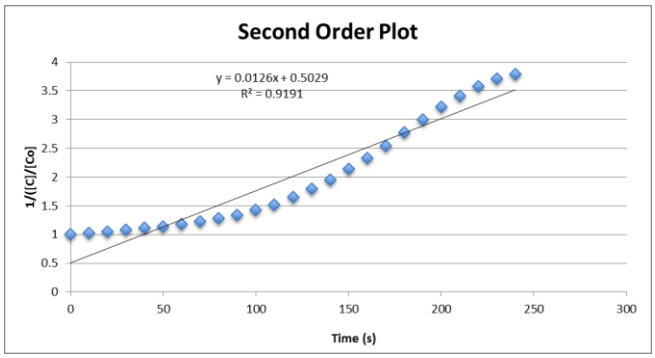

Figure 52: Second Order Plot from IPO Experiment on GDI E30 PM at 510°C